Ion-combination specific effects driving enzymatic activity of halophilic Alcohol Dehydrogenase 2 from *Haloferax volcanii* in aqueous ionic liquid solvent mixtures

Alexandra Schindl,*[a,b,c,d,e] M. Lawrence Hagen,[a] Christof M. Jäger,[f,a] Andrew C. Warden,[g] Mischa Zelzer,[b] Thorsten Allers,[c] Anna K. Croft*[h]

[a]*Sustainable Process Technologies group, Department of Chemical and Environmental Engineering, University of Nottingham, Nottingham NG7 2RD, United Kingdom*

[b]*School of Pharmacy, University of Nottingham, University Park Campus, Nottingham NG7 2RD, United Kingdom*

[c]*School of Life Sciences, University of Nottingham, Queen's Medical Centre, Nottingham NG7 2UH, United Kingdom*

[d]*School of Molecular and Cellular Biology, University of Leeds, Leeds LS2 9JT, United Kingdom*

[e]*Astbury Centre for Structural Molecular Biology, Faculty of Biological Sciences, University of Leeds, Leeds LS2 9JT, United Kingdom*

[f]*Data Science and Modelling, Pharmaceutical Sciences, R&D, AstraZeneca Gothenburg, Pepparedsleden 1, SE-431 83 Mölndal, Sweden*

[g]*CSIRO Environment, Commonwealth Scientific and Industrial Research Organization (CSIRO), Research and Innovation Park, Acton, Canberra, ACT, 2600, Australia*

[h]*Department of Chemical Engineering, Loughborough University, LE11 3TU, United Kingdom*

Abstract

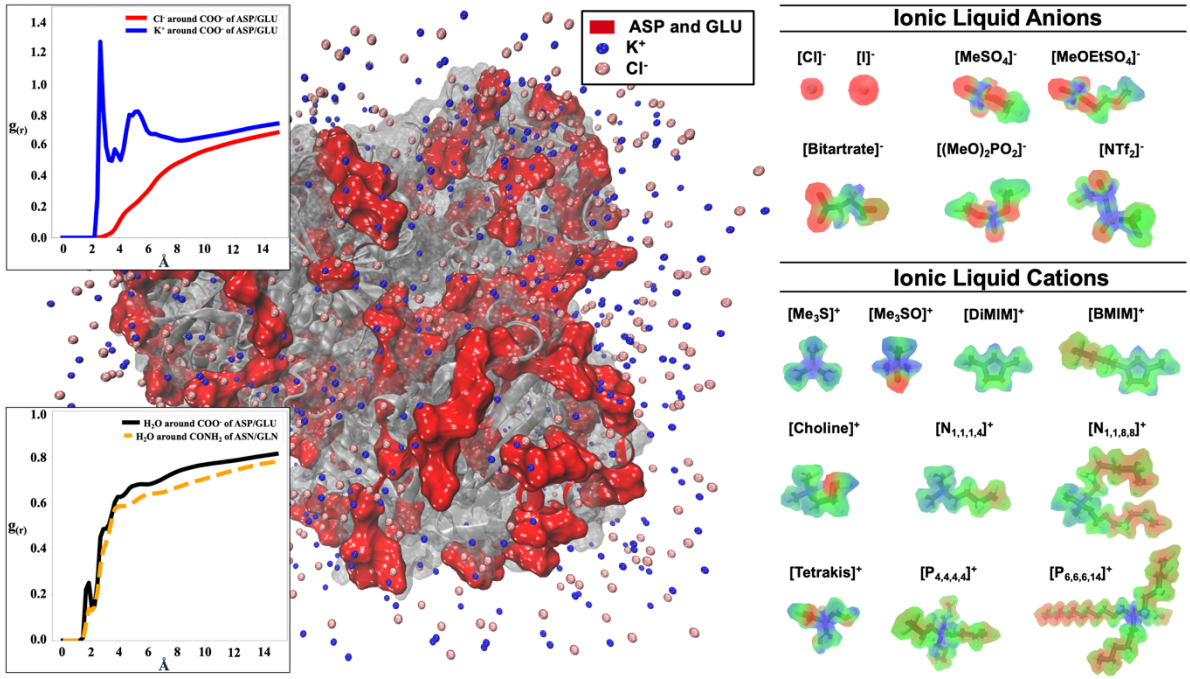

Biocatalysis in ionic liquids enables novel routes for bioprocessing. Enzymes derived from extremophiles promise greater stability and activity under ionic liquid (IL)

influence. Here, we probe the enzyme Alcohol Dehydrogenase 2 from the halophilic archaeon *Haloferax volcanii* in thirteen different ion combinations for relative specific activity and analyse the results against MD simulations of the same IL systems. We probe the ionic liquid property space based on ion polarizability and molecular electrostatic potential. Using radial distribution functions, survival probabilities and spatial distribution functions of ions we show that cooperative ion-ion interactions determine ion-protein interaction, specifically, strong ion-ion interactions equate to higher enzymatic activity if neither of the ions interact strongly with the protein surface. We further demonstrate a tendency for ions interacting with the protein surface to be least detrimental to enzymatic activity if they show a low polarizability and a small range of molecular electrostatic potential. We also find that the IL ion influence is not mitigated by the surplus of negatively charged residues of the halophilic enzyme. This is shown by free energy landscape analysis in root mean square deviation and distance variation plots of active site gating residues (Trp43 and His273) demonstrating no protection of specific structural elements relevant to preserving enzymatic activity. On the other hand, we observe a general effect across all IL systems that a tight binding of water at acidic residues is preferentially interrupted at these residues through the increased presence of potassium ions.

Overall, this study demonstrates a co-ion interaction dependent influence on allosteric surface residues controlling the active/inactive conformation of halophilic Alcohol Dehydrogenase 2 and the necessity to engineer ionic liquid systems for enzymes that rely on the integrity of functional surface residues regardless of their halophilicity or thermophilicity for use in bioprocessing.

Introduction

Environmentally benign routes to replace existing chemical processes are a high priority to achieve a sustainable and circular economy. Enzymes can be deployed as biocatalysts for the synthesis of pharmaceuticals, biofuels, fine chemicals, and other industrially relevant molecules. [1, 2] Biocatalytic processes are often less energy demanding, as well as polluting than traditional chemical synthetic processes since they function under temperatures and pressure below the boiling point of water, they are selective and have good specificity towards substrate and product, and the catalysts themselves are renewable. [3, 4] To ensure good uptake of biocatalytic solutions into industry, however, drawbacks such as catalyst instability, difficulties with dissolution of/access to substrates, and product recovery need to be addressed.

The use of ionic liquids (ILs), solvents that are composed of ions yet are liquid at temperatures below < 100 °C, have shown great promise in enhancing biocatalytic outcomes. [5, 6] There are now many studies highlighting how enzyme stability can be improved through the application of ILs, [7, 8] the advantages conferred by improvements in solubility mediated by the tunability of solvation properties of the ILs [9, 10], and how ILs allow for novel mechanisms for product recovery. [11, 12] Combined with the process advantages of ILs, [13] these solvents are attractive to further expand the breadth of chemistries available to bioprocessing. However, exact mechanisms for the interaction between ionic liquid ions and proteins remain not fully understood and finding an adequate system wherein a given biocatalyst remains stable and soluble remains challenging. For this, biocatalysts derived from extremophilic organisms are of substantial interest as they remain functional under harsh conditions, such as high temperatures, [14] extreme pH [15] or salinity, [16] without being specifically engineered. Hence, extremozymes (enzymes derived from extremophiles) act as promising initial candidates for enzyme engineering where challenging reaction conditions are necessary.

To maximise the scope of biosynthetic outcomes, a combination of approaches can be beneficial. Bioprocesses harnessing the inherent properties of halophilic proteins are so far scarce, with the most successful example combining ionic liquids and halophilic cellulases in the saccharification of pretreated lignocelluloses. (For examples see: [17-23]. Studies of a halophilic protease from *Salinivibrio sp.*, [24] a halophilic phenylalanine dehydrogenase from *Natranaerobius thermophiles* [25] and an

engineered halophilic malate dehydrogenase [26] found ionic liquid systems wherein the enzyme showed increased activity compared to the free enzyme. Halophilic organisms thrive in high salt environments and have adapted their proteins to intracellular molar concentrations of salt. Main structural adaptations are an excess of negatively charged residues located at the protein surface and a reduction of aromatic hydrophobic residues in the core, [27, 28] however the exact mechanism how increased salt tolerance is conferred remains unclear. Halophilic proteins might thus be expected to be an existing match to avoid problems with ionic liquid compatibility that are seen in mesophilic enzymes.

This study focuses on the industrially significant enzyme alcohol dehydrogenase, here from the archaeal species *Haloferax volcanii* (*Hv*ADH2). The archaeal enzyme has been previously found to exert a preference for haloalkaliphilic conditions (4 M KCl, pH 10) when catalysing the oxidative conversion of alcohol substrates to ketones or aldehydes, and slightly acidic (pH 6) for the catalysis of the reductive reaction [29]. It exhibits a remarkable thermoactivity with a maximum at 90 °C and its binding pocket can accommodate bulky substrates. [30] Under bioprocess conditions, pH can be controlled to allow for the tuning of the reaction equilibrium in favour of the desired product. Glycine-KOH buffer has been routinely used to characterise *Hv*ADH2. [29] The same buffer conditions have been used to characterise enzymatic activity in a range of organic solvents and the enzyme demonstrated remarkable resilience, specifically in dimethyl sulfoxide and methanol. [31] Commercially, the use of co-solvents is a necessity for certain reactions to afford maximum yields and in this case, if sparingly water-soluble ketones are to be used as substrates, they are indispensable. Substitution of organic co-solvents with ionic liquids that can be more easily recycled and endure higher temperatures therefore has good potential for industrial adaptation. A broad range of different IL ions acting as co-solvent additives were investigated and are depicted in Figure 1. With regards to MD simulations, these ions represent a wider physicochemical space to study interactions between surface residues and biocatalyst structure and ionic liquid ions than has been to date reported in literature. [32-51]
We report here both experimental results and extensive molecular dynamics simulations that together shed light on some of the key interactions and considerations needed when using ionic liquid co-solvents, including specific complexities of halophilic systems.

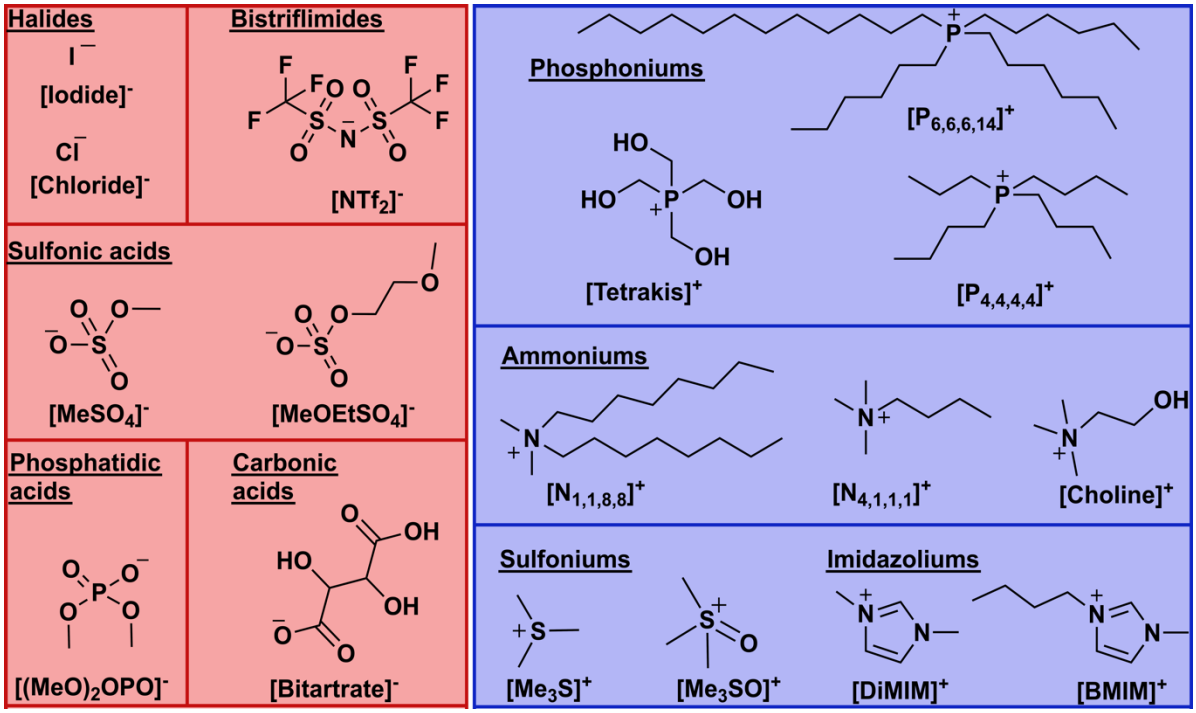

Figure 1. Structures of ionic liquid ions used in this work. Cation classes comprise phosphonium, ammonium, sulfonium and imidazolium ions **(blue)**. Anions comprise halides, bistriflimides, sulfonic acids, phosphatidic acids and carbonic acids **(red)**.

Results and Discussion

Selection of ionic liquids

To effectively probe ion-protein interactions we selected a range of ions and ion combinations according to the two ion descriptors, polarizability and the range of the molecular electrostatic potential (MEP_{range}). Both have been shown to be of great importance to IL ion behaviour in solution, at surfaces, and in directly influencing reaction kinetics. [25, 52, 53] Ion descriptor combinations are depicted in Figure 2. Anions were selected based on their increasing polarizability, starting with monatomic anions $[Cl]^-$ and $[I]^-$, followed by $[MeSO_4]^-$, $[(MeO)_2OPO]^-$, [Bitartrate]$^-$, $[MeOEtSO_4]^-$ and $[NTf_2]^-$ in this order. Anions were then combined with different cations diverging in their polarizability and/or MEP_{range}. Cations included two imidazolium cations ($[DiMIM]^+$ and $[BMIM]^+$), hydroxyl-functionalised cations ([Tetrakis]$^+$ and [Choline]$^+$), sulfonium based small hydrocarbon cations ($[Me_3S]^+$ and $[Me_3SO]^+$), and phosphonium or nitrogen based cations with medium-to-long alkyl chains ($[N_{1,1,1,4}]^+$, $[N_{1,1,8,8}]^+$, $[P_{4,4,4,4}]^+$ and $[P_{6,6,6,14}]^+$). Through these combinations we have covered a majority of the descriptor

space. A detailed description of these combinations is given in the SI, Ionic liquid descriptor space.

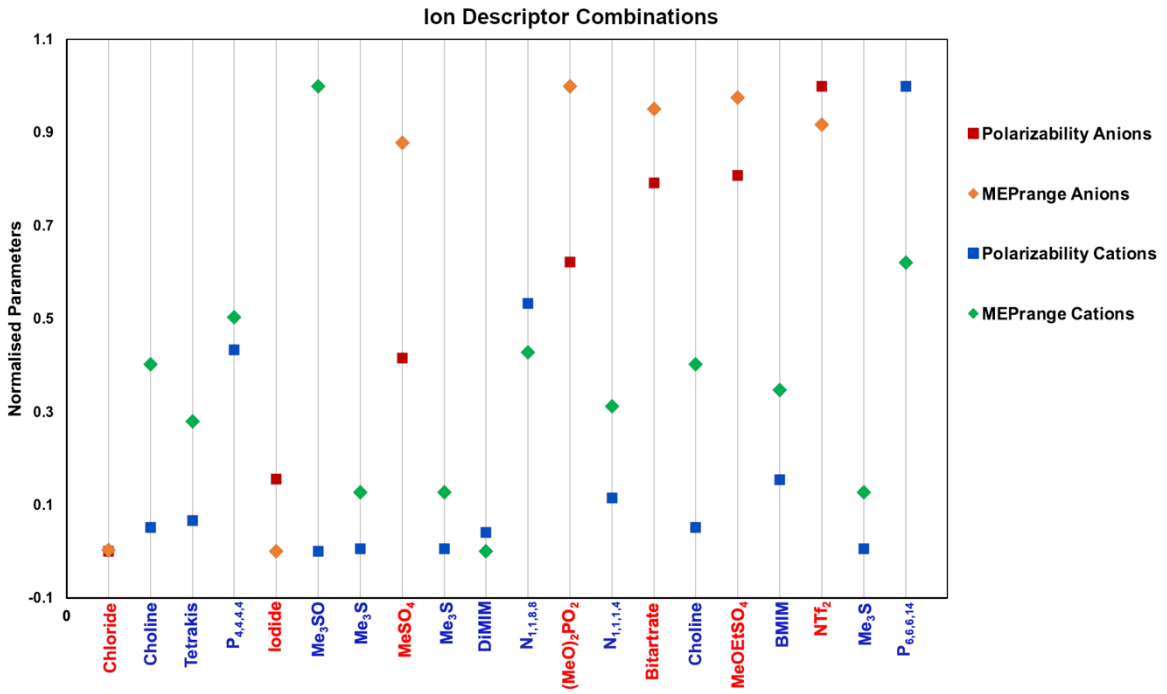

Figure 2. Normalised ion descriptors 'Polarizability' and 'MEP_{range}' from anions and cations calculated with Empire show descriptor distribution across ions. Anions are followed by their respective cations to show descriptor combinations across ion pairs.

Activity of *Hv*ADH2 in aqueous ionic liquid solvent systems

Initially, ion-protein interactions were determined by measuring the effect of added ILs on enzyme activity. The relative specific activity of *Hv*ADH2 was assayed by monitoring the formation of NADPH using UV spectroscopy. Assays containing ILs were compared to native conditions measured in a Glycine-KOH buffer at pH 10 containing 4 M KCl at 50 °C. Glycine-KOH buffer was used to make up IL-aqueous mixtures for experimental assays, since it has been routinely used in previous studies. [29, 31] These results were compared with MD simulations incorporating the enzyme in aqueous solution with added KCl and ionic liquid of the corresponding concentration to be able to focus the analytic comparison on the specific effects of different ILs. Those comparisons demonstrate good agreement between systems showing a high/low enzymatic activity and IL ion interaction trends observed for survival probability and radial distribution from MD simulations, presented below. The salt content of 4 M KCl and pH 10 was not varied for MD simulations.

Ionic liquid concentrations of 25 mM, 150 mM and 750 mM were assayed for $[Me_3S]^+[MeSO_4]^-$, [Tetrakis]$^+$[Cl]$^-$, [Choline]$^+$[Cl]$^-$, [DiMIM]$^+[MeSO_4]^-$, $[Me_3S]^+[NTf_2]^-$, $[N_{4,1,1,1}]^+[(MeO)_2OPO]^-$, $[P_{6,6,6,14}]^+[NTf_2]^-$ and $[Me_3S]^+[I]^-$. Ionic liquids [Choline]$^+$[Bitartrate]$^-$, $[BMIM]^+[MeOEtSO_4]^-$, $[N_{1,1,8,8}]^+[MeSO_4]^-$, $[P_{4,4,4,4}]^+$[Cl]$^-$ and $[Me_3SO]^+[I]^-$ were not soluble at a concentration of 750 mM as well as IL $[P_{4,4,4,4}]^+$[Cl]$^-$ at a concentration of 150 mM and hence were not measured at these concentrations. For a detailed composition of mixtures see SI, Preparation of ionic liquid mixtures.

Results of spectrophotometric assays are shown in Figure 3. The activity results for *Hv*ADH2 are consistent with studies reporting inhibitory effects by imidazolium ions on ADH enzymes. [54, 55] Sulfonate ions $[MeSO_4]^-$ and $[MeOEtSO_4]^-$ are herein found to be detrimental for *Hv*ADH2 activity too, despite reports of improvements on conversion rates for ADHs in $[MTEOA]^+[MeSO_4]^-$, $[AMMOENG^{TM}100]^+[MeSO_4]^-$ and $[AMMOENG^{TM}102]^+[EtSO_4]^-$, as well as $[EMIM]^+[MeSO_3]^-$ and [Tris-(2-OH-Et)-MAM]$^+[MeSO_4]^-$, respectively. [56, 57] Sulfonium based ions on the other hand appear compatible with *Hv*ADH2, since *Hv*ADH2 showed the highest tolerance in ionic liquids $[Me_3S]^+[MeSO_4]^-$ and $[Me_3S]^+[I]^-$, consecutive only to an exceptional activity increase of ~ 150 % in $[P_{6,6,6,14}]^+[NTf_2]^-$. Thus, additional concentrations were measured for these three IL systems. This revealed that enzymatic activity in $[Me_3S]^+[MeSO_4]^-$ and $[P_{6,6,6,14}]^+[NTf_2]^-$ does not follow a continuous decrease with increasing ionic liquid concentration. Activity in $[Me_3S]^+[MeSO_4]^-$ plateaued between 150 mM and 300 mM, albeit activity was decreased for both compared to the lower concentrations of 25 mM and 75 mM, and activity diminished to below 10 % at 600 mM $[Me_3S]^+[MeSO_4]^-$. Despite the formation of an emulsion for all concentrations, the enzymatic activity in $[P_{6,6,6,14}]^+[NTf_2]^-$ also followed a non-continuous concentration dependence. Enzymatic activity decreased between 25 mM and 75 mM but increased at 150 mM compared to 75 mM and increased further at 300 mM, where enzymatic activity was highest. In comparison with $[Me_3S]^+[MeSO_4]^-$ and $[P_{6,6,6,14}]^+[NTf_2]^-$, enzymatic activity decreased continuously with increasing concentration for $[Me_3S]^+[I]^-$. Another water immiscible IL, $[BMIM]^+[NTf_2]^-$ has been previously reported to enhance enantioselectivity of an ADH by lowering the concentration of substrate in the aqueous phase. [58] Similarly, equilibria for the oxidative reaction of ADH2 might be most ideal at a concentration of ~ 300 mM IL. Multiple studies have found ADH activity enhanced at very low IL concentrations of different ions but dropping particularly rapidly at higher concentrations. [57, 59] A study on a zinc finger protein proposed a transition point in

water structuring, affecting electrostatic interactions and residence times of ions at the protein surface and consequentially, the secondary structure of the protein. [42, 60, 61] The same mechanism could underlie the observed increase in activity for $[P_{6,6,6,14}]^+[NTf_2]^-$, and could also help explain the non-linear decrease in activity in $[Me_3S]^+[MeSO_4]^-$ at 300 mM. As such, a molecular-level insight is likely to prove valuable in teasing out these possibilities but will require a comparison of different concentrations of IL.

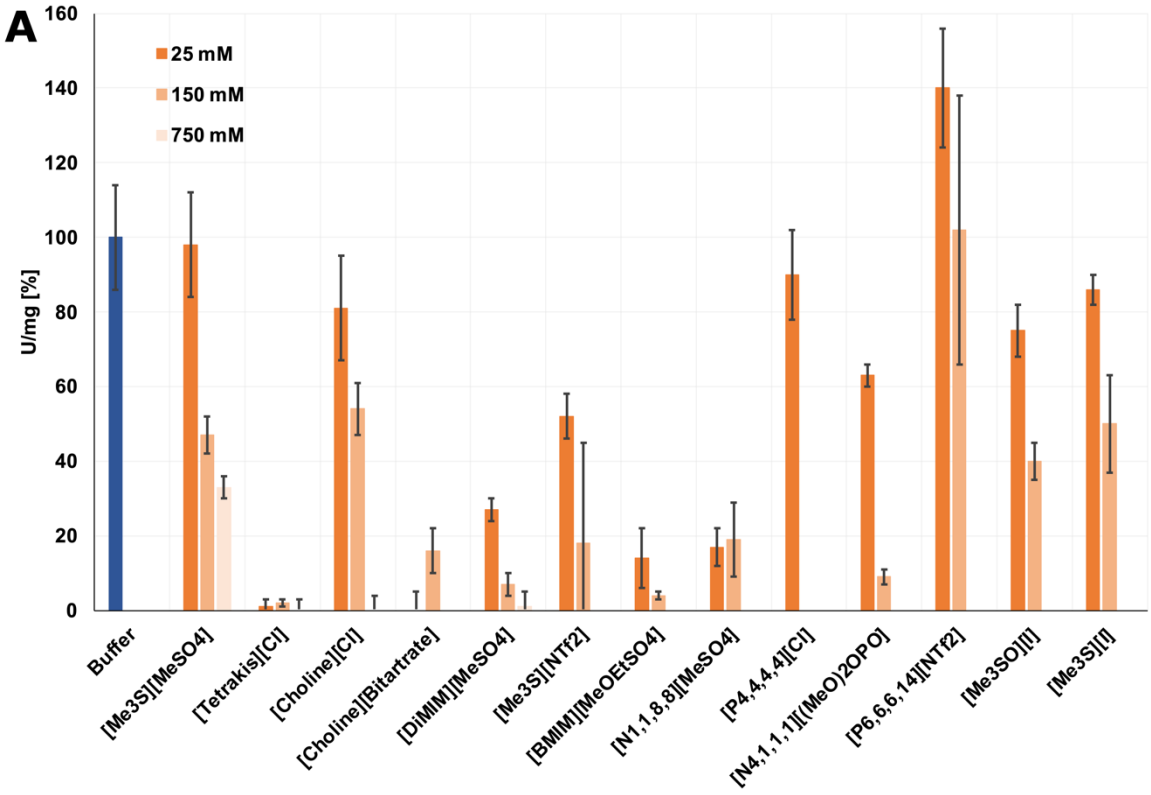

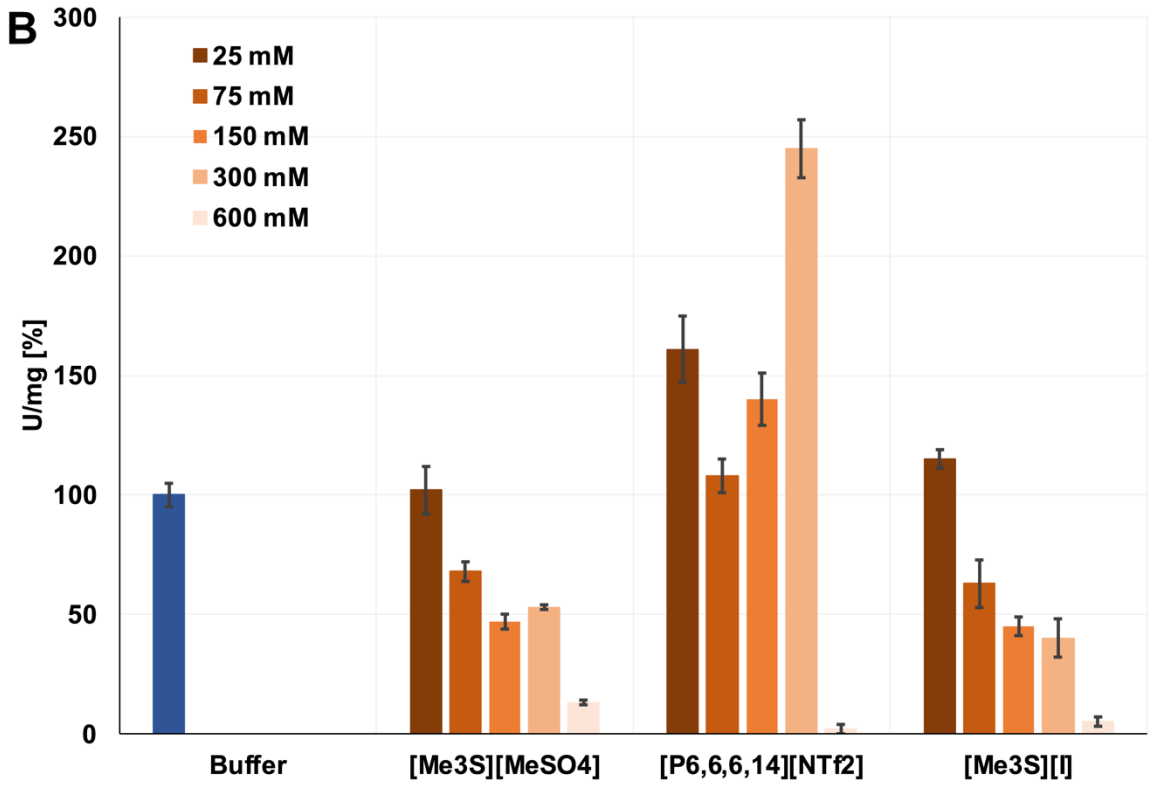

Figure 3. Relative specific activities of *Hv*ADH2 in buffer (blue) and in ionic liquid mixtures (orange-hues) of **(A)** three concentrations (25 mM, 150 mM and 750 mM) for all ionic liquid mixtures (duplicates, error bars indicate estimated standard deviations) and **(B)** five concentrations (25 mM, 75 mM, 150 mM, 300 mM and 600 mM) for the three best performing ionic liquid mixtures (triplicates, error bars indicate standard deviations) are shown. At the lowest concentration of 25 mM $[Me_3S]^+[MeSO_4]^-$ showed no adverse effect on the relative specific activity of *Hv*ADH2. Enzymatic activity was above 80 % for $[Choline]^+[Cl]^-$, $[P_{4,4,4,4}]^+[Cl]^-$, $[P_{6,6,6,14}]^+[NTf2]^-$, $[Me_3SO]^+[I]^-$ and $[Me_3S]^+[I]^-$ at 25 mM, above 50 % for $[Me3S]^+[NTf_2]^-$ and $[N_{4,1,1,1}]^+[(MeO)_2OPO]^-$ and was reduced to above 10 % for $[DiMIM]^+[MeSO_4]^-$, $[BMIM]^+[MeOEtSO4]^-$ and $[N_{1,1,8,8}]^+[MeSO_4]^-$. $[Tetrakis]^+[Cl]^-$ inhibited enzymatic activity exclusively at all concentrations measured.

MD Simulations

The protein surface introduces higher ordering of molecules within the solvation shell and K^+- COO^- interaction mediates solvent structure

First, we investigated the influence of molar concentrations of K^+ and Cl^- on the solvation of the protein, in particular, on negatively charged residues. We used radial distribution functions (RDFs) and spatial distribution functions (SDFs) to characterize the solvent structure surrounding the protein within a 10 Å cutoff. The spatial structuring of water and ions surrounding *Hv*ADH was calculated over a simulation time of 120 ns after the systems had equilibrated (total simulation time 200 ns). We observe that K^+ ions disrupt the solvation shell around surface COO^- functionalities,

while solvated K^+ ions associate directly and in a prolonged fashion to internal COO^- functionalised residues. Interactions of potassium ions and water with Glu and Asp residues are summarised in Table 1, and exemplify the strong organisation imparted by the protein surface.

Table 1. Average association distances (peaked) between carboxylic acid residues (COO^-), K^+ and H_2O in Angstrom [Å], abstracted from radial distribution functions (SI Figure S1): K^+ and H_2O around Glu and Asp residues, H_2O around Gln and Asn, K^+ and H_2O (K^+-O_W) and between K^+ ions (K^+-K^+).

Interaction	1st assoc. dist. Å	2nd assoc. dist. Å	3rd assoc. dist. Å	4th assoc. dist. Å
COO^- – K^+	2.7	3.7-4.3	4.3 – 6.0	–
COO^-– H_2O	1.5 – 2.1	2.9 – 3.1	3.3 – 4.1	4.1 <
K^+ – H_2O	2.9	3.3	4.5 – 6.5	–
K^+ – K^+	3.5 – 5.3	5.7 – 6.3; 6.5 – 7.3	7.9 – 8.5	–
H_2O – H_2O	2.5	5.1 – 7.1	–	–

At the protein surface as well as in bulk solvent we find a distinct first solvation shell for O_W- O_W, indicating greatest probability between water molecules at ~ 2.5 Å, which is followed by a second broader and less pronounced shell, peaking at ~ 5.5 Å (SI Figure S1). A slight reduction of the first association distance is observed closer to the protein surface. A study in the context of a system of free-floating aspartic acid molecules by Lenton *et al.* found a disappearance of the second coordination shell at higher concentrations of KCl, indicating that the tetrahedral structure of water was disrupted. [62] Other crystallographic observations support this and show, that surface acidic residues disrupt pentagonal water networks in the hydration shell. [63] Contrary to this, analysis of the solvent structure and its interaction with the protein surface from crystallised halophilic glucose dehydrogenase suggested higher complexity in the first and second solvation shell, which is reflected in a most ordered arrangement of pentagonal rings of water molecules around distinct sites. [64] However, crystallising conditions might distort solvation shells and ion coordination. Compared to the profile found by Lenton *et al.* in low salt, the second peak for O_W- O_W found in this study is farther removed from the protein surface by ~ 1 Å, but conversely is still present, unlike in Lenton's profile for high salt. These discrepancies suggest that the presence of the protein surface aids conservation of higher complexity in the water structure even at distances of up to 25 Å from the surface.

The here observed ion hydration at the protein surface differs from literature-reported ion hydration around individual amino acids. [62] Lenton *et al.* observed two peaks in the RDF plot for K- O_W, whereas we find three peaks, indicating a split of the first peak into two solvation shells due to the presence of the protein surface. We also find a higher ordering into better defined shells of K^+ arrangements at the protein surface (15 Å) compared to the profile of K^+- K^+ within 100 Å, as can be inferred from a smoother profile for the latter, and a greater dispersion of K^+ ions close to the protein surface (< 10 Å) (SI Figure S1).

The RDF between potassium and carboxylate groups of Asp/Glu residues determined in this study (SI Figure S1 and S2) matches the same positions for all three coordination shell peaks as found in a study by Warden *et al.*, constituting sodium ions in various salts at the surface of an engineered halo-tolerant carbonic anhydrase. [65] The RDF profile of O1- K of free-floating aspartic acid from the Lenton *et al.* study on the other hand shows only one pronounced peak in both low and high salt conditions with diverging profiles at greater distances, highlighting the influence of the presence of the protein surface on structural arrangements of smaller molecules. Finally, RDF distances between O_W and C4/C5 of Asp/Glu, respectively, match solvation shells found at protein surfaces reported in literature. [66] However, we observe an increase in probability for the first coordination shell at ~ 2 Å compared to non-halophilic CALB [66] as well as at non-acidic surface residues of *Hv*ADH2, see SI Figure S2. This observation fits with literature which suggests that the carboxylic side chains of Asp and Glu residues have pK_a values of 4.0 and 4.4 in 0.0 M salt respectively, which in high salt (5 M) rise to 4.9 (Asp) and 5.3 (Glu), thereby increasing the strength of the hydrogen bond between water and Asp/Glu. [62] This is supported by crystal structures that show increased water binding for halophilic proteins with an average of 1.9 water molecules per residue, compared to an average of 1.2 in mesophilic proteins. [16] However, it was pointed out that under crystallizing conditions salt exclusion and improved water binding is expected, suggesting a misrepresentation of native conditions. [67]

Our study suggests increased water binding takes place at charged residues when compared to uncharged, polar residues on the protein surface of *Hv*ADH2. All 237 negatively charged residues (17 % of total *Hv*ADH2 residues), except one Glu per monomer, are located on the surface of the homo-tetramer, facilitating the possibility of increased water content over the whole protein surface. Indeed, visualisation of the

calculated probability densities around charged residues (Figure 4), and around uncharged residues (SI Figure S3) indicate coordination of water structure by K^+ at the protein surface regardless of charge. For instance, coordination of water around Thr1073 by K^+ demonstrates these site-specific influences particularly well (SI Figure S3). However, the solvation shell around uncharged residues is less tightly bound than that surrounding negatively charged residues, as can be seen by comparing visualisations in Figure 4 and SI Figures S3 and S4, and RDFs in SI Figure S2. K^+ ions specifically interrupt the solvation shell around negatively charged residues, i.e. 'pull' water molecules from the negatively charged surface without necessarily directly associating with the surface themselves (Figure 4; B and SI Figure S4; A,B,C), albeit not in all cases (Figure 4; D, E and SI Figure 4; D), and rarely replace water molecules in a direct interaction (Figure 4; A,C). The presence of high charge density salts is presumed to cause electronic repulsion of solutes and enhance the 'hydrophobic effect', [68-70] which comes at the cost of loss of configurational flexibility/a higher entropic penalty, leading to a highly ordered structure of the solvent at non-polar solute-water interfaces. [71] For polar and water-soluble solutes, the relative contributions of electronic repulsion and the hydrophobic effect are less well understood. However, fully water-solvated states, as observed in salting-out conditions will be disfavoured due to the large entropic penalty. As mentioned above, calculated solvation profiles of water around mesophilic proteins show much less water content in the first (< 2 Å) and second (< 3 Å) solvation shells. Taken together, our findings suggest that the presence of K^+ ions around negatively charged residues 'breaks', or rather, mediates the solvation shell, and, through the increased number of acidic residues, allows a cumulative effect to off-set salting-out conditions through localised ion association. The highly structured water shell surrounding the protein is thereby disrupted and the protein is allowed greater flexibility in high salt conditions.

The observed direct interaction (~ 2.7 Å) between K^+ ions and specific, buried Glu residues (Figure 4; A) is established over a prolonged time. Moreover, the very same K^+ ions stay associated to Glu1292 in monomer D, as well as its equivalent in monomer A, Glu245, over the whole trajectory, see SI Figure S5. These K^+ ions in turn coordinate water molecules, which stay associated for about half the trajectories before being exchanged (SI Figure S5). Corresponding residue Glu594 in monomer B does not coordinate a K^+ at all over the course of the trajectory, while Glu943 in monomer C interacts multiple times with different potassium ions but is unable to capture one. By

comparison, acidic surface residues exchange their K^+ frequently (every few fs). This frequent exchange is underpinned by the Lenton *et al.* study where the interaction strength between potassium and the side-chain carboxylate oxygen decreases with increasing salt. However, the coordination numbers stay the same, suggesting a higher surface mobility on part of the cations. [62] We found, that in the native *Hv*ADH2 system the decay of K^+ around Glu and Asp is slower by approximately a factor of 4 compared to its decay around positively charged residues (SI Figure S11), thus indicating a prolonged interaction between K^+ ions and acidic residues. However, we have no comparison to low salt conditions. Interestingly, sodium ions around carboxylate groups of amphiphilic micelles were shown to bind preferentially over potassium ions with a ratio of 2.75:1 within the first hydration shell. [72, 73] This could serve as a possible explanation why halophilic archaea preferentially accumulate potassium over sodium intracellularly to combat osmotic pressure in high salt environments. [74] Sodium ions may rigidify protein structure similarly to micelles. [73] Water has a similar short permanence time (survival probability) around negatively or positively charged residues, indicating that the dynamics (mobility) of the water network is not altered by the prolonged presence of K^+ ions at carboxylate groups (SI Figure S11).

Taken together our findings demonstrate an increased presence of water molecules at negatively charged residues, which are coordinated by a stark elevated presence of K^+ ions at carboxylate groups. This suggests a mechanism where K^+ ions serve to displace water molecules without necessarily directly interacting with negatively charged residues, however, thereby offsetting any order solvent structure of water at the protein surface in high salt, which would trap the enzyme.

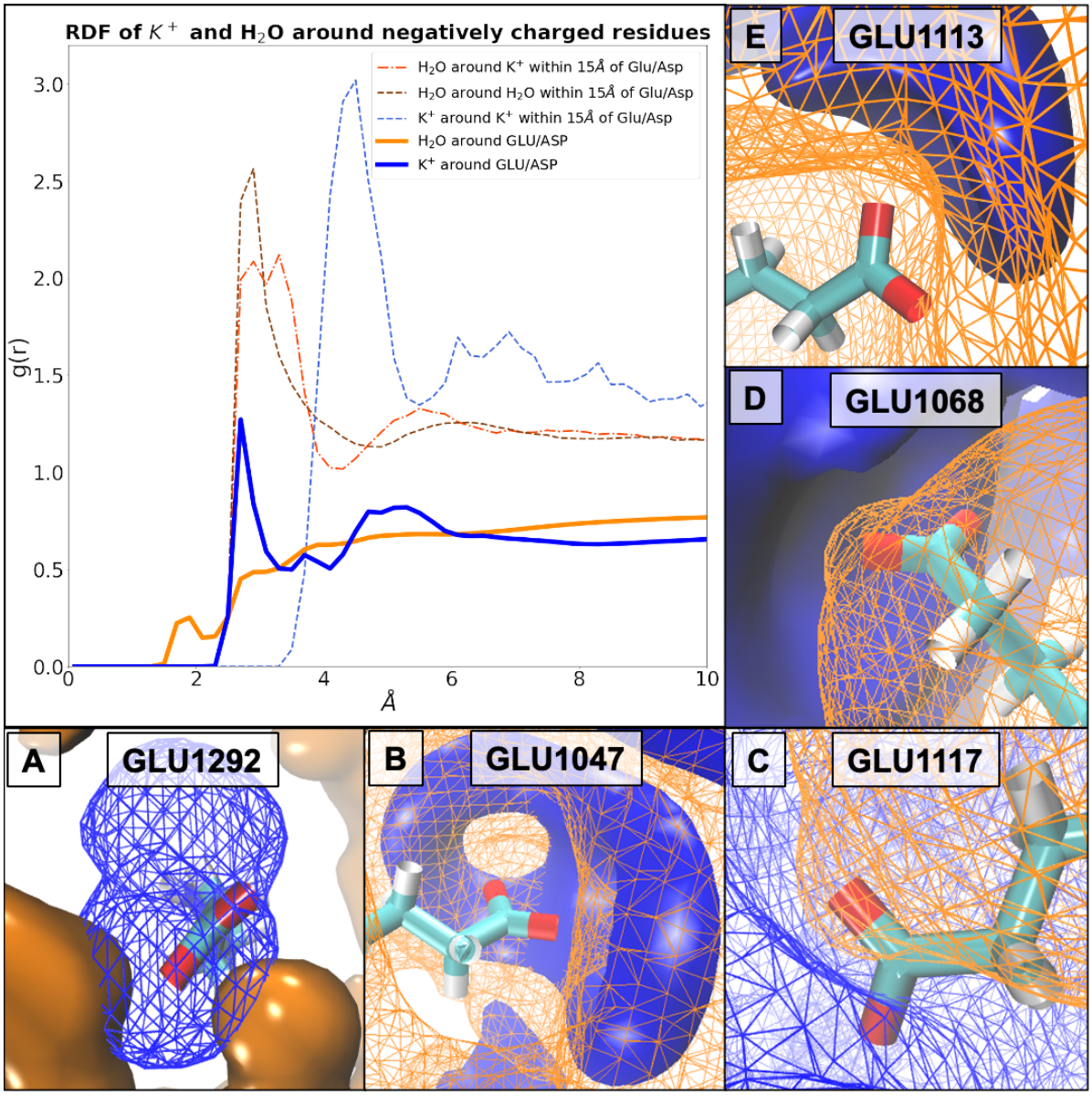

Figure 4. Plotted RDFs and visualised SDFs of K^+(blue mesh or solid) and H_2O (orange mesh or solid) molecules surrounding carboxylic acid residues in the native *Hv*ADH2 system. **(A)** Direct association of K^+ to COO^- occurs. Directly associated K^+ at 2.7 Å may account for the distance of the second hydration shell of H_2O around COO^- at 2.9-3.1 Å consistent with the distance between K^+ and H_2O in their first hydration shell at 2.9 Å. **(B)** Neither K^+ nor H_2O associate directly. Hydration of COO^- is established by the fourth association distance of H_2O at > 4.1 Å, since H_2O molecules get pulled towards the associated K^+ ions. **(C)** Direct association of water to COO^- at 1.5-2.1 Å may account for the second coordination shell of K^+ around COO^- at 3.7-4.3 Å, in concordance with the first hydration shell of H_2O around K^+ of 2.9 Å. **(D)** No direct association takes place. K^+ ions either strip H_2O molecules partially from COO^- residues or are themselves removed behind a water barrier**. (E)** Direct association of water in its second hydration shell at 2.9 Å to COO^- may associate K^+ ions according to the fourth association distance between H_2O and K^+ at 4.5 Å.

Cooperative ion- ion interactions increase or decrease interaction with protein residues and compare to relative activities from experimental assays

After inferring solvent interactions specific to halophilic proteins, we investigate the influence of IL ion pairing specific interactions on solvent- and IL- protein interactions. Spatial correlations and residence time of ions and water around protein residues in ionic liquid solutions were studied through RDFs and survival probability (SP) analysis. SP allows an estimate on how long molecules remain in proximity to another. SP between anions and respective cations, their individual SPs at the protein surface as well as RDFs between ions and their individual RDFs around the protein surface allow an estimate on how the interaction between ions influences the interaction of individual ions with the protein surface. A generalised summary of our findings is depicted in Figure 5. Plotted RDFs and SPs of IL ions are shown in SI Figures S6, S8 and S9.

First, the influence of IL ions on the spatial correlations and residence times of K^+/ Cl^- ions and the solvation shell around *Hv*ADH2 were evaluated by RDFs and SPs analyses. Compared to the native system, SP of K^+ ions around acidic residues is decreased in all IL systems and increased for all ILs around basic residues, except for hydroxy-functionalised ILs, where it is slightly decreased (SI Figure S14). RDFs of K^+ ions in IL systems show the same profile as the native system, but $g_{(r)}$ values are increased for all ILs around negatively charged residues and slightly increased around basic residues (SI Figure S12), while Cl^- ions are slightly removed from basic as well as acidic residues (SI Figure S13). Taken together this indicates that all IL systems influence the dynamics of K^+ around charged residues leading to faster dynamics and a greater total number of K^+ surrounding negatively charged residues, while mitigating dynamics between K^+ and positively charged residues. SP of H_2O around acidic as well as basic residues is decreased for all IL systems (SI Figure S15). RDFs of H_2O are decreased for all systems around acidic residues, around K^+ ions and between H_2O molecules (SI Figure S10). In this, the dynamics of H_2O are altered in all IL systems similarly, becoming generally faster, and molecules become more dispersed.

Regarding ionic liquid ions our results are summarised as follows: SP of anions around cations declined with hydrophobicity, steric bulkiness and charge localisation, in the order: $[P_{6,6,6,14}]^+[NTf_2]^-$ > $[N_{1,1,8,8}]^+[MeSO_4]^-$ > $[P_{4,4,4,4}]^+[Cl]^-$ > $[BMIM]^+[MeOEtSO_4]^-$ >

$[N_{4,1,1,1}]^+[(MeO)_2OPO]^-$ > $[Me_3S]^+[NTf_2]^-$ > $[DiMIM]^+[MeSO_4]^-$ > [Choline]$^+$[Bitartrate]$^-$ > [Tetrakis]$^+$[Cl]$^-$ > $[Me_3S]^+[MeSO_4]^-$ > $[Me_3S]^+[I]^-$ ~ $[Me_3SO]^+[I]^-$ > [Choline]$^+$[Cl]$^-$.

RDFs of anions around cations decline in this order: $[P_{6,6,6,14}]^+[NTf_2]^-$ > $[N_{1,1,8,8}]^+[MeSO_4]^-$ > $[Me_3S]^+[NTf_2]^-$ > $[DiMIM]^+[MeSO_4]^-$ > $[N_{4,1,1,1}]^+[(MeO)_2OPO]^-$ > $[Me_3S]^+[MeSO_4]^-$ > $[BMIM]^+[MeOEtSO_4]^-$ > [Choline]$^+$[Bitartrate]$^-$ > $[Me_3S]^+[I]^-$ ~ $[Me_3SO]^+[I]^-$ > [Choline]$^+$[Cl]$^-$ > [Tetrakis]$^+$[Cl]$^-$ > $[P_{4,4,4,4}]^+$[Cl]$^-$.

SPs of cations around *Hv*ADH2 decline in the following order: $[BMIM]^+$ > [Tetrakis]$^+$ ~ $[P_{4,4,4,4}]^+$ > $[N_{1,1,8,8}]^+$ > $[N_{4,1,1,1}]^+$ > $[DiMIM]^+$ > $[P_{6,6,6,14}]^+$ > [Choline]$^+$ ([Cl]$^-$) > [Choline]$^+$ ([Bitartrate]$^-$) > $[Me_3S]^+$ ($[NTf_2]^-$) > $[Me_3SO]^+$ ($[I]^-$) ~ $[Me_3S]^+$ ($[I]^-$) > $[Me_3S]^+$ ($[MeSO_4]^-$) and SPs of anions decline as follows: $[I]^-([Me_3S)]^+$ > $[I]^-$ ($[Me_3SO)]^+$ > $[NTf_2]^-$ ($[Me_3S]^+$) > $[MeSO_4]^-$ ($[Me_3S)]^+$ > $[MeSO_4]^-$ ($[DiMIM]^+$) > $[MeSO_4]^-$ ($[N_{1,1,8,8}]^+$) > $[MeOEtSO_4]^-$ > [Bitartrate]$^-$ > $[(MeO)_2OPO]^-$ > $[NTf_2]^-$ ($[P_{6,6,6,14}]^+$) > [Cl]$^-$ ([Tetrakis]$^+$ ~ $[P_{4,4,4,4}]^+$ ~ [Choline]$^+$).

Literature reports, through dielectric measurements, that in solvated ionic liquids solvent-assisted ion pairs are much more common than direct contact ion pairs or aggregates. [75, 76] We observe for ions that have a 'strong' interaction with another, reflected in a high SP (close to 1) and a high RDF (probability of finding a molecule at a certain proximity), a co-joined interaction with the protein surface, which modulates the overall interaction with protein residues, while the influence of individual ions on the protein surface is greater for ions that share a low SP (close to 0) and low RDF with one another. For example, while the strong hydrophobic interaction between $[P_{6,6,6,14}]^+$ and $[NTf_2]^-$ (high SP and RDF) shields the anion from the protein surface, the comparatively decreased interaction with the cation $[Me_3S]^+$ allows $[NTf_2]^-$ to strongly interact with positive residues and the protein surface. This is demonstrated in SI Figure S6, for comparison see systems $[P_{6,6,6,14}]^+[NTf_2]^-$ and $[Me_3S]^+[NTf_2]^-$. The strong interaction between $[P_{6,6,6,14}]^+$ and $[NTf_2]^-$ matches a much higher relative specific activity. By comparison, SP between $[MeOEtSO_4]^-$ and $[BMIM]^+$ is the highest (decays to ~ 0.3, see SI Figure S8) of all non-emulsion-forming systems (RDF is lower because only ion pairs, and not micro-heterogenic aggregates, [77] are formed), but because both ions interact strongly with the protein surface ($[BMIM]^+$ highest SP of all presented ions, $[MeOEtSO_4]^-$ highest RDF of all presented ions, see SI figures S9 and S6 respectively), their synergistic effect on the protein appears to be detrimental, since a greatly diminished relative activity (< 5 U/mg [%] at 150 mM) is observed for this system. Small anions of hydrophilic ILs were shown to interact as mediators between

water molecules and cations, which are to some extent expelled and form clusters similar to micelles. [78] We find this to be in agreement with our systems $[DiMIM]^+[MeSO_4]^-$ and $[Me_3S]^+[MeSO_4]^-$ forming small ion patches, with system $[Me_3S]^+[I]^-$ and $[Me_3SO]^+[I]^-$ forming loose ion pairs and for $[P_{4,4,4,4}]^+[Cl]^-$ where cations form bigger patches and occasionally interact strongly with chloride ions (lowest RDF, 3rd highest SP, see SI Figure S8). The formation of multi-ion structures is driven by entropic forces, since apolar domains minimise the disturbance of the H-bond network of the water molecules. This surfactant effect gets stronger, the longer the cationic alkyl chain and this can affect the stability and activity of proteins positively through suppression of protein-protein interactions, preventing aggregation. [79] However, if coulombic interactions between ions are strong and moreover if such ions are substituted with hydrophobic tails, strong dispersion forces are observed. [79] While this does not have immediate implications for proteins if these ion clusters are located in bulk solvent, it is likely that such ions are expelled from the hydrogen bond network at interfaces and may act as surfactants for solvated proteins. We find this to be the case for systems $[N_{1,1,8,8}]^+[MeSO_4]^-$, $[P_{4,4,4,4}]^+[Cl]^-$, $[DiMIM]^+[MeSO_4]^-$ and $[N_{4,1,1,1}]^+[(MeO)_2OPO]^-$, which form small patches all over the protein surface as observed from MD simulations. These systems show a decreased enzymatic activity, while $[P_{6,6,6,14}]^+[NTf_2]^-$, which forms one big patch which interacts only localised with the protein surface as observed in MD simulations, see SI Figure S19, increases activity. Increased activity could here be attributed to suppression of protein-protein interactions and this particular IL might be well suited for bioreactor formulation. [80]

RDF profiles of ions around *Hv*ADH2 diverge from each other in terms of distance and magnitude of solvation shells and are detailed in SI Figure S6. Anions intruding onto the protein surface below 1.9 Å are: $[MeOEtSO_4]^-$ > $[Bitartrate]^-$ > $[MeSO_4]^-$ ~ $[(MeO)_2OPO]^-$ > $[NTf_2]^-$($[Me_3S]^+$) and cations intruding below 1.9 Å are: $[Tetrakis]^+$ > $[Choline]^+$($[Bitartrate]^-$) > $[Choline]^+$($[Chloride]^-$) > $[N_{1,1,8,8}]^+$.

Taken together it is difficult to say that ions of matching polarizability and MEP_{range} have a positive impact on enzyme activity. While this is true for $[P_{6,6,6,14}]^+$ $[NTf_2]^-$, $[Choline]^+[Chloride]^-$, $[Me_3S]^+[I]^-$ and $[Me_3SO]^+[I]^-$, the ion pairings $[DiMIM]^+[MeSO_4]^-$ and $[Tetrakis]^+[Chloride]^-$, having also similar polarizability and MEP_{range}, are detrimental to enzymatic activity. Their functional groups enable them to specifically interact with the protein via $\pi-\pi$ stacking or hydrogen-bond interactions as observed in MD simulations, see SI figure S19. Having similar polarizability and MEP_{range} is also

non-beneficial for $[N_{1,1,8,8}]^+[MeSO_4]^-$, where the surfactant effect of $[N_{1,1,8,8}]^+$ draws $[MeSO_4]^-$ to the surface of the protein, rather than removes it, as is seen for the system of unmatching polarizability and MEP_{range}, $[Me_3S]^+[MeSO_4]^-$, which shows good enzymatic activity.

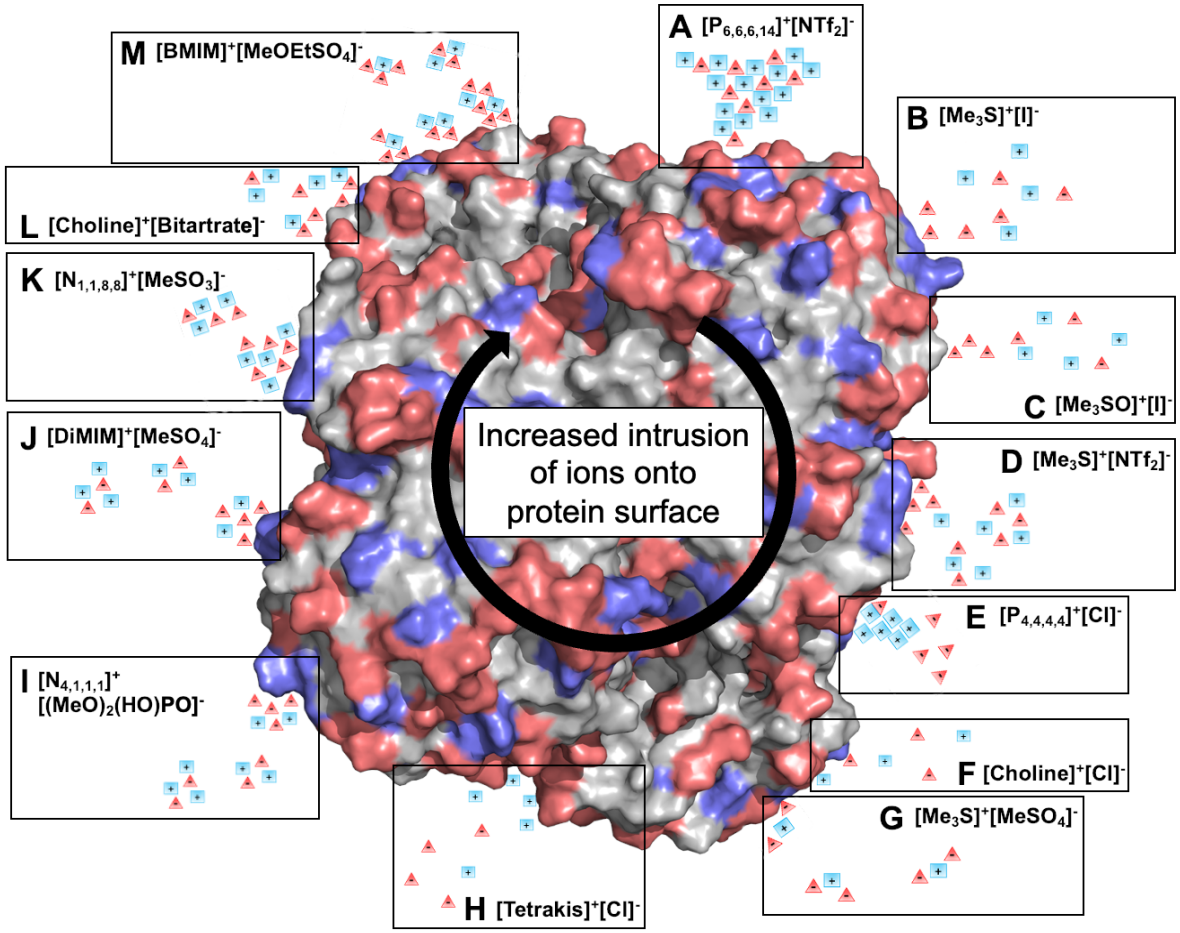

IL pair	Start of RDF coordination shell [Cation / Anion] [Å]	Highest observed g(r) [Cation / Anion]	RDFs ranked*	SPs ranked~
$[P_{6,6,6,14}]^+[NTf_2]^-$	2.2 / 2.2	0.4 / 0.4	1	1
$[Me_3S]^+[I]^-$	2.0 / 2.5	0.7 / 3.1	9	11
$[Me_3SO]^+[I]^-$	2.0 / 2.5	0.7 / 3.0	10	12
$[Me_3S]^+[NTf_2]^-$	2.0 / 1.8	0.9 / 3.5	3	6
$[P_{4,4,4,4}]^+[Cl]^-$	1.9 / 2.0	2.0 / 0.5	13	3
$[Choline]^+[Cl]^-$	1.4 / 2.0	1.2 / 0.5	11	13
$[Me_3S]^+[MeSO_4]^-$	2.0 / 1.5	0.7 / 2.1	6	10
$[Tetrakis]^+[Cl]^-$	1.3 / 2.0	2.0 / 0.5	12	9
$[N_{4,1,1,1}]^+[(MeO)_2OPO]^-$	1.8 / 1.5	1.4 / 2.4	5	5
$[DiMIM]^+[MeSO_4]^-$	1.9 / 1.5	1.2 / 3.3	4	7
$[N_{1,1,8,8}]^+[MeSO_4]^-$	1.9 / 1.5	1.3 / 3.1	2	2

[Choline]$^+$[Bitartrate]$^-$	1.3 / 1.3	1.1 / 2.8	8	8
[BMIM]$^+$[MeOEtSO$_4$]$^-$	1.9 / 1.0	1.9 / 3.9	7	4

* RDFs between anions and cation - 1 equals highest g(r)
~ SPs between anions and cations - 1 equals highest/longest

Figure 5 and Table 2. Summary of the general trend of ion-protein and ion-ion interaction inferred from RDFs and SPs and observations from trajectories. Negatively charged residues and anions (triangles) are shown in red, positively charged residues and cations (squares) in blue. Tabulated values are taken from SI figures S6 and S8. **(A)** Anions and cations of ionic liquid [$P_{6,6,6,14}$]$^+$[NTf_2]$^-$ form one big hydrophobic patch that occasionally interacts with a part of the protein surface. **(B+C)** [Me_3S]$^+$ and [Me_3SO]$^+$ cations and [I]$^-$ anions interact as loose ion pairs. [I]$^-$ ions paired with [Me_3S]$^+$ associate slightly more to charged residues than [I]$^-$ ions paired with [Me_3SO]$^+$, but interaction to uncharged surfaces is the same for both systems. **(D)** [NTf_2]$^-$ ions in this pairing show the second highest RDF value around basic residues of all IL ions and because [NTf_2]$^-$ anions and [Me_3S]$^+$ cations form ion patches, RDF values for [Me_3S]$^+$ are increased for this system in comparison to when [Me_3S]$^+$ is paired with [I]$^-$ or [$MeSO_4$]$^-$. **(E)** Although the interaction between [$P_{4,4,4,4}$]$^+$ and [Cl]$^-$ is long-lived (third highest SP of all ions), it is a rare encounter (lowest RDF of all ions). [$P_{4,4,4,4}$]$^+$ ions form hydrophobic patches that associate all over the protein surface, while [Cl]$^-$ are mostly excluded, but associate to positive residues in a distinct shell. **(F+H+L)** Hydroxyl-functionalised ions [Choline]$^+$, [Tetrakis]$^+$ and [Bitartrate]$^-$ intrude below the solvation shell and interact with counter-charged protein residues. The association of ions to residues increases with an increased number of OH groups. [Choline]$^+$ [Bitartrate]$^-$ interact as ion pairs, while [Choline]$^+$ and [Tetrakis]$^+$ interact as loose ion pairs with [Cl]$^-$ ions (RDF slightly higher between [Choline]$^+$ [Cl]$^-$, SP slightly higher for [Tetrakis]$^+$[Cl]$^-$). **(G)** [Me_3S]$^+$ is mostly paired with two [$MeSO_4$]$^-$. With the exception of hydrophobic ILs, ions of this system associate least to the protein surface (overall low RDF). **(I+J+K)** Ions of the systems [$N_{4,1,1,1}$]$^+$[$(MeO)_2OPO$]$^-$, [DiMIM]$^+$[$MeSO_4$]$^-$ and [$N_{1,1,8,8}$]$^+$[$MeSO_4$]$^-$ form ion patches. The anion intrudes below the solvation shell around positively charged residues. While the sulfonate ions draw their respective cations slightly closer to the protein surface, the RDF of [$(MeO)_2OPO$]$^-$ to protein is overall lower compared to [$MeSO_4$]$^-$ in both systems, while the RDF of [$N_{4,1,1,1}$]$^+$ to protein is increased compared to [DiMIM] and [$N_{1,1,8,8}$]$^+$. The system [$N_{4,1,1,1}$]$^+$[$(MeO)_2OPO$]$^-$ is also the only system where anions and cations show almost equal RDF profiles, with the exception of the sytem [$P_{6,6,6,14}$]$^+$[NTf_2]$^-$.

Interaction of IL ions with active-conformation-gating residues and co-factor coordination is prevalent for all IL systems. Highly dynamic and highly static IL ion interactions match higher activity in experimental assays

In a separate step we focus on the influence of IL ions on extremophilic ADH-specific structural elements and investigate ion pairing specific interactions with activity-conferring residues. Flexibility of the tetramer and the tendency for unfolding in ILs was analysed by inspecting free-energy landscapes (FELs) of the different IL systems. FELs represent the conformational space the enzyme adopts during simulation. A

higher number of separated minima indicates greater flexibility, but if the barrier between minima is low, it is an indication of a transition into non-native and possibly non-active states. The native system of ADH2 descends into multiple local higher energy minima before occupying the final lowest minimum. The second lowest minimum is separated via a higher energy bridge and local minima from the lowest minimum, indicating a stabilisation of the structure followed by structural rearrangements into higher energy states before its final descend. All IL systems force *Hv*ADH2 into non-native states (SI Figure S16). The general trend shown by the native system is preserved for all IL systems except for $[Me_3SO]^+[I]^-$, and is best preserved by $[Me_3S]^+[MeSO_4]^-$. ILs can be grouped into those preventing ADH2 from visiting stabilising minima before its final descend ([Choline]$^+$[Bitartrate]$^-$, $[DiMIM]^+[MeSO_4]^-$, $[BMIM]^+[MeOEtSO_4]^-$, $[P_{4,4,4,4}]^+[Cl]^-$, $[P_{6,6,6,14}]^+[NTf_2]^-$, $[Me_3SO]^+[I]^-$) and those that show a broadening and an increased number of throughs of local minima ($[Me_3S]^+[MeSO_4]^-$, [Tetrakis]$^+$[Cl]$^-$, [Choline]$^+$[Cl]$^-$, $[Me_3S]^+[NTf_2]^-$, $[N_{1,1,8,8}]^+[MeSO_4]^-$, $[N_{4,1,1,1}]^+[(MeO)_2OPO]^-$, $[Me_3S]^+[I]^-$). The former appear to trap *Hv*ADH2 in non-native states and latter appear to de-stabilise the native state.

Protein conformations from final minima were inspected for the interaction between residues determining the active/inactive conformation of the enzyme. Work from Klinman *et al.* identified residues (Trp49 and Phe272) within a thermophilic ADH (*ht*ADH) from *B. stearothermophiles* to be involved in a π-stacking interaction that has direct effect on the active site microenvironment. [81] These residues are not directly located at the proteins' active site but on the surface, connecting homo-monomers. Upon closer inspection of the *Hv*ADH2 structure, a similar π-stacking interaction was found between residues Trp43 and His273, albeit within the same monomer (Figure 6 and SI Figure S17). This interaction was found to correlate to the open, or inactive, state of *Hv*ADH2 in the native system and appears to stabilise the apo-enzyme. MD simulations were started with three of the four subunits having NAD^+ bound and over the course of the trajectory NAD^+ dissociated from two of the three subunits, whereby only one subunit expelled the cofactor completely (monomer C). Figure 6 shows the inactive conformation of monomer A from which dissociation of NAD^+ takes place at the beginning of the trajectory. Both vanguard residues Trp43 and His273 are involved in guiding the cofactor through π-stacking out of the binding pocket. In a first step His273 pulls the ribose-ring of NAD^+ out of the immediate vicinity of the catalytic zinc, followed by a take-over of NAD^+ by Trp43 through the interaction with the pyridinium

ring of NAD^+. NAD^+ is then passed back to His273 via the ribose-ring and released into an outer cavity on the surface of the nicotinamide binding domain (NBD), where it stays for the rest of the trajectory. After NAD^+ is expelled, residues His273 and Trp43 assume the π-stacking interaction, which stays undisturbed until the end of the trajectory. In comparison, monomer D remains as a holo-enzyme during the whole simulation and residues Trp43 and His273 assume the structural arrangement shown in SI Figure S17; B.

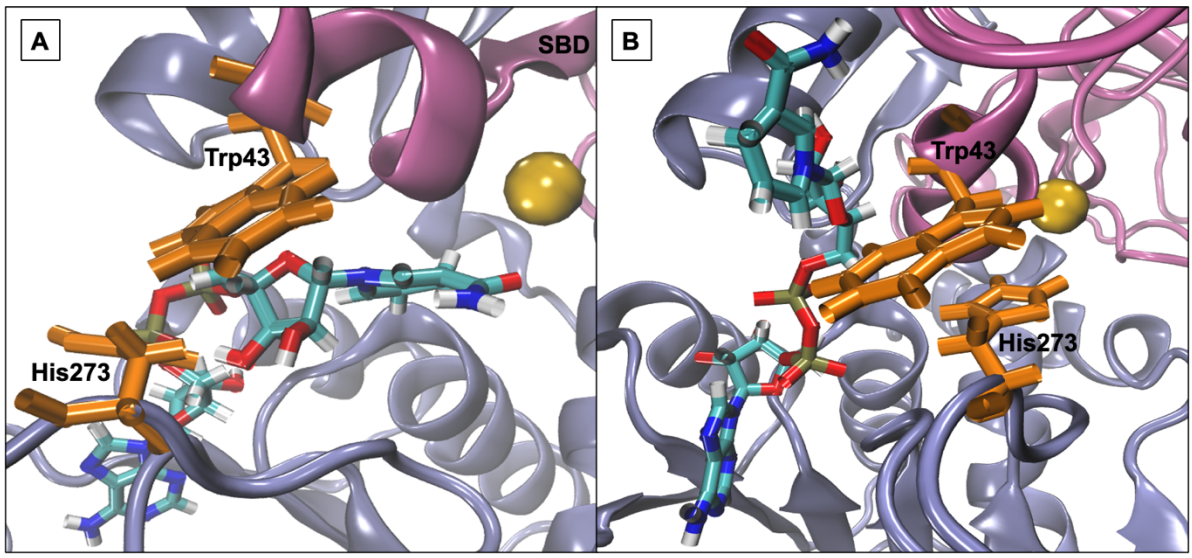

Figure 6. Residues Trp43 and His273 in monomer A of the native HvADH2 system jointly coordinate NAD+ out of the binding pocket. Coordination starts at around 10ns, and expelling the co-factor is complete after around 20ns. However, Pi-stacking between vanguard residues is only established at around 100ns. **(A)** NAD^+ is coordinated in the vicinity of the nicotine binding domain (NBD) (iceblue) in close proximity to the catalytic zinc, which is located in the substrate binding domain (SBD) (mauve). **(B)** NAD^+ has been expelled from the catalytic cleft and residues Trp43 and His273 have assumed the π-stacking interaction.

The change in distance between the two vanguard residues was analysed and plotted over the course of the trajectory of the native system and compared to IL containing systems. Results are shown in SI Figure S18. The change in distance of the residues in the native system reflects the dissociation of NAD^+ for monomer A, where rearrangements are greatest in the beginning of the trajectory until expulsion of NAD^+, when the π-stacking interaction fixates the distance between Trp43 and His273 for the rest of the trajectory. For monomer D change in distance between Trp43 and His273 remains roughly constant throughout the trajectory.

All ionic liquids studied directly interfere/coordinate with Trp43 and/or His273 and/or NAD^+ (within 7 Å). Coordination of IL ions and changes in bond distance between residues Trp43 and His273 are shown for all systems in SI Figure S18. Systems wherein ions associate for a prolonged time to vanguard residues or NAD^+ correlate with lower relative activity from activity assays. $[Tetrakis]^+$ cations, for example, coordinate throughout the trajectory to NAD^+ and stay associated up to a third of the trajectory (~ 60 ns) (SI Figure S19). The longest interaction was found for $[N_{4,1,1,1}]^+$ cations, which interacted with Trp43 for > 100 ns within monomers A and D (SI Figure S19). Contrary to this, distance mapping between sulfonium ions and vanguard residues showed high mobility for $[Me_3SO]^+$ and $[Me_3S]^+$ in the systems paired with $[I]^-$. These ions were found in frequent proximity (> 10 Å) to vanguard residues and the catalytic zinc, however direct coordination was less frequent and lasted below 10 ns, as is shown in Figure 7. However, $[Me_3S]^+$ showed also a 100 ns long interaction with Trp43 in the system wherein it is paired with the anion $[NTf_2]^-$, highlighting again the influence of relative anion-cation interaction strengths on ion-protein interactions.

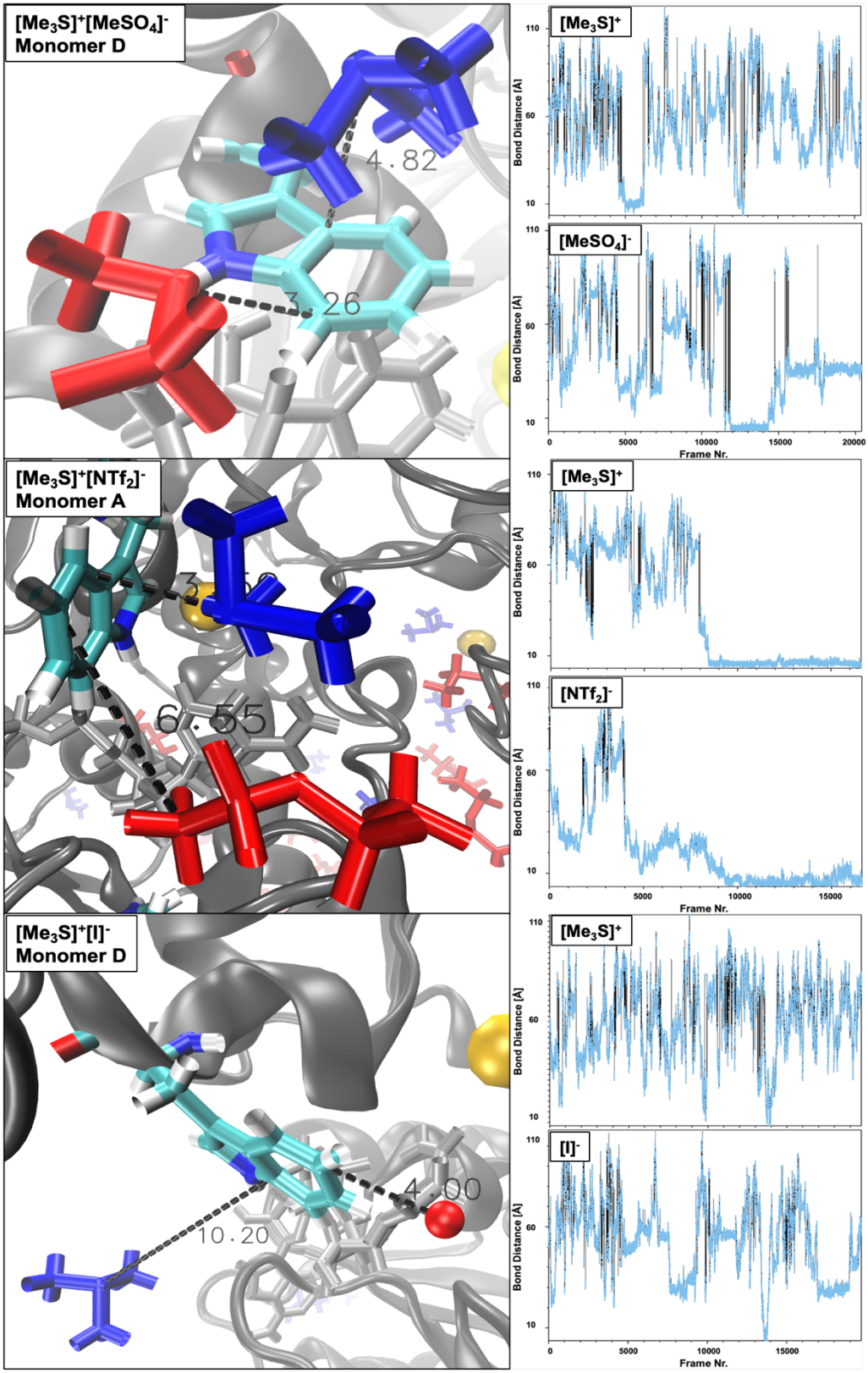

Figure 7. Distances between IL cations (blue) and anions (red) and gating residue Trp43 are depicted, and plotted over the course of the trajectory. Cartoon representation show tetrameric *Hv*ADH2 in ILs $[Me_3S]^+[MeSO_4]^-$ **(top)**, $[Me_3S]^+[I]^-$ **(middle)** and $[Me_3S]^+[I]^-$ **(bottom)**. Plots demonstrate the difference in interaction of cation $[Me_3S]^+$ within the different systems and its dependence on its counter-ion.

ILs compromise structural integrity of protein salt bridge networks

The total number of intra-protein salt-bridges of the tetramer with an O- N distance cut-off of 3.2 Å was calculated for the native system and IL systems. All ILs lead to an increase in the total number of salt-bridges, (Table 2), but native salt-bridges are not necessarily conserved, (SI data). This suggests an interruption of the native salt-bridge network in all IL systems and a distortion of the secondary and tertiary structure of *Hv*ADH2. This finding is consistent with a MD study on lactalbumin in different concentrations of $[BMIM]^-[BF_4]^+$, which found an increase in numbers of salt bridges with increasing concentration of IL, and an increased strength of the salt bridge bond. [47] However, while their study finds increased rigidity through the increase in salt bridges, also reflected in a restrained RMSD, we find decreased rigidity of the protein backbone, reflected in a less restrained RMSD (SI Figure S21). Inter-subunit salt bridges have been shown to be increased for halophilic proteins when compared to mesophilic counterparts [82-84] and it was suggested that oligomerisation acts as a stabilisation mechanism in extremophiles. [67] Interruption of native salt bridges is therefore likely to have a different effect on the halophilic salt bridge network, than on the mesophilic one. If oligomerisation via a tertiary structure-stabilising mechanism of halophilic proteins is matched to a specific level of ionic strength, breaking of salt bridges conferring oligomerisation due to varying ionic strength will also lead to a disintegration of tertiary structure. We find an increase in backbone RMSD, which suggests greater flexibility of the tetrameric and tertiary structure.

Table 3. Number of total protein residue salt bridges calculated by VMD from MD simulations of HvADH2 within the native system in high salt (4 M KCl) in comparison to IL systems.

System	Total intra-protein salt-bridges (increasing order)
Native (4 M KCl)	313
$[N_{4,1,1,1}]^+$ $[(MeO)_2OPO]^-$	319
$[Tetrakis]^+$ $[Cl]^-$	322
$[Choline]^+$ $[Bitartrate]^-$	322
$[Me_3S]^+$ $[NTf_2]^-$	322
$[Me_3SO]^+$ $[I]^-$	322
$[P_{4,4,4,4}]^+$ $[Cl]^-$	327
$[N_{1,1,8,8}]^+$ $[MeSO_4]^-$	329
$[Me_3S]^+$ $[I]^-$	333

$[BMIM]^+ [MeOEtSO_4]^-$	335
$[Me_3S]^+ [MeSO_4]^-$	336
$[P_{6,6,6,14}]^+ [NTf_2]^-$	340
$[DiMIM]^+ [MeSO_4]^-$	351

Conclusion

A combination of experimental assays and analysis of MD simulations has provided insight into the hydration and ionic interaction of halophilic *Hv*ADH2 in both salt and ionic liquid solutions. We observe tight binding of hydration water around carboxylic acid residues, consistent with previous reports, [62, 63, 85, 86] in addition to a selective breaking of water structure induced by the coordination of potassium around carboxylic acid residues. Breaking of polygonal water networks by acidic residues has been reported previously, wherein it was suggested that solvation-stabilisation, i.e. a preferential binding of water to acidic residues over water-water interaction lends halophilic proteins their solubility in high salt. [63] Our results show that water structure is specifically broken at carboxylic acid residues coordinating potassium, whereas water structure is unbroken around polar residues, despite potassium coordination. In addition, the water network remains unbroken and no potassium coordination occurs around positively charged and apolar surface residues. In support of the previously proposed solvation-stabilisation model, [67] we propose that the specific ionic interaction of potassium to tightly hydrated carboxylic acid residues is responsible for maintaining protein flexibility in high salt concentrations. Our findings suggest that carboxylic acid residues recruit water molecules to solvate the protein, while at the same time their coordination of potassium prevents a ‘trapping’ of the protein within a hydration shell.

We further find that the increase in negatively charged residues of halophilic protein surfaces cannot protect enzymatic activity from the influence of IL ions. Unlike potassium interacting specifically with carboxylated residues, IL ions interact with the protein surface depending on both their physico-chemical properties and their inter-ion interactions. Depending on the function of the halophilic protein, IL ions might be generally more or less detrimental. Halophilic cellulases for example stay mainly unaffected [87] and these then have an advantage to be deployed as biocatalysts in preference to mesophilic cellulases, within a given set of ionic liquids favourable to

dissolving the relevant substrates. For enzymes such as dehydrogenases that have a less robust catalytic mechanism, which depends very much on the integrity of their quaternary structure (the *Hv*ADH2 homo-dimer is around two thirds less active than the homo-tetramer under native conditions) [29] and for which the active and inactive conformations rely on the functionality of specific residues located on the surface of the protein, a fine-tuning of IL ions is required in the same way for halophilic as well as non-halophilic proteins.

Our results demonstrate that cooperative ion-ion interactions determine ion-protein interactions and can be related to enzymatic activity. Strong inter-ion interactions, as is the case for $[P_{6,6,6,14}]^+[NTf_2]^-$, can be harnessed to favour biocatalytic processes. Here, phase separation means the protein is mainly excluded from the hydrophobic patch of the IL, whilst maintaining the advantages of either a reservoir of dissolved hydrophobic substrate or removal of hydrophobic products from the solvent to push the reaction equilibrium in the favoured direction. While this system led to the highest observed enzymatic activity, it is comprised of ions with highest polarizability and a high MEP_{range}. As a general trend however, a low polarizability and a low MEP_{range} of ions seems to be less detrimental to enzymatic activity of *Hv*ADH2. Systems $[Me_3S]^+[MeSO_4]^-$, $[Me_3S]^+$[Iodide]$^-$, [Choline]$^+$[Cl]$^-$, $[Me_3SO]^+$[Iodide]$^-$ and $[P_{4,4,4,4}]^+$[Cl]$^-$, showing low polarizability, rank best in terms of enzymatic activity behind the superior system $[P_{6,6,6,14}]^+[NTf_2]^-$. This latter system is hydrophobic and interacts only little with the protein surface. However, another explanation could be anion diffusion. Anion diffusion was shown to be slowed down in bulk-like regions of high polarizability [52]. Hence, the high polarisability and bulk-like properties of $[P_{6,6,6,14}]^+$ could lead to an altered dynamic of $[NTf_2]^-$. Unfortunately, no further systems here investigated were comprised of both ions showing high polarizability. However, when $[NTf_2]^-$ is paired with the minimally polarized cation, $[Me_3S]^+$, enzymatic activity is decreased, despite a strong ion-ion interaction, and presence of $[NTf_2]^-$ at the protein surface is increased. A weak interaction between ions appears to be favourable where both ions act in favour of protein activity either by themselves or in combination, as is the case for ILs $[Me_3S]^+[MeSO_4]^-$, $[Me_3S]^+[I]^-$ and $[Me_3SO]^+[I]^-$. This suggests, that small, highly dynamic cations with low polarisability and small charge-dense anions can help preserve catalytic activity in our system. In addition, the atomic structure of the ions plays an equally important role. The presence of the planar structure of the minimally

polarisable cation $[DiMIM]^+$ lead to a 5-fold decrease in enzymatic activity when compared to the tetrahedral structure possessing and comparably low polarisable cation $[Me_3S]^+$, when both are paired with $[MeSO_4]^-$. Further, when $[MeSO_4]^-$ is paired with the highly polarisable cation $[N_{1,1,8,8}]^+$ enzymatic activity is similarly impaired. Finally, ion-water interactions negatively affected protein-water interactions in all IL systems and hydroxy-functionalised ILs did not stabilise the surrounding water network. Indeed, hydroxy-functionalised systems performed worst of all ILs when multiple functionalised groups were present, with only $[Choline]^+[Cl]^-$ performing well. This may be due to increased protonation/deprotonation events at the protein surface [88] or may be a more general outcome for all ILs due to ion type dependent alignment of water at interfaces. [89]

Taken together, our data highlights the tuneability of the influence of ions on protein activity depending on co-ion interaction. The same anion or cation may exhibit a different influence on the protein when paired with a different co-ion, mainly depending on the strength of ion-ion interaction. The quality of ion-ion interactions in turn depends on polarizability and the resulting molecular electrostatic potential. We find that, for halophilic proteins, ions with low polarizability are better suited to maintaining activity, however, ion structure and ion-ion interactions need to be taken into account.

Author Contributions

Authors' Contribution statement: **Alexandra Schindl:** Conceptualisation (equal), Formal Analysis (lead), Investigation (lead), Visualisation (lead), Methodology (lead), Writing – Original Draft Preparation (lead), Writing – Review and Editing (equal); **M. Lawrence Hagen:** Formal Analysis (support), Visualisation (support); **Christof M. Jäger**: Methodology (support), Writing – Review and Editing (equal), **Andrew C. Warden:** Methodology (support), **Mischa Zelzer:** Conceptualisation (equal), Supervision (equal), Writing – Review and Editing (equal), **Thorsten Allers:** Conceptualisation (equal), Supervision (equal), Methodology (support), Writing – Review and Editing (equal), **Anna K. Croft:** Conceptualisation (equal), Supervision (equal), Writing – Original Draft Preparation (support), Writing – Review and Editing (equal)

Conflicts of Interest

There are no conflicts to declare.

Acknowledgements

The authors would like to gratefully acknowledge the support of the BBSRC/EPSRC Synthetic Biology Research Centre – Nottingham (BB/L013940/1) and the University of Nottingham for the financial support provided to AS, and the BBSRC for the award of a Doctoral Training Grant (BB/M008770/1, Nottingham-Rothamsted Doctoral Training Partnership) for MLH. AKC would like to gratefully acknowledge the support of a Leverhulme Trust Research Fellowship (RF-2022-625). AS gratefully thanks Ricardo Parra-Cruz for assistance with Free Energy Landscape calculations and discussions, and Jennifer Cassidy for assistance and advice on protein purification, as well as Karin S. Schaffarczyk McHale for supplying a manual on IL ion preparation for MD simulation. The work was further supported by access to the University of Nottingham's High Performance Computing Facility.

Materials and Methods

Reagents and culture conditions. All chemical reagents, unless stated otherwise, were purchased as analytical grade from Sigma-Aldrich. All restriction enzymes were purchased from New England Biolabs. Standard molecular cloning techniques were used. PCR amplification used Q5® Hot Start High-Fidelity DNA Polymerase. *H. volcanii* strains were grown at 45 °C on complete (*Hv*-YPC) or Cas-amino acids (*Hv*-Ca) agar or broth as described previously. [90] Isolation of genomic and plasmid DNA as well as transformation of *H. volcanii* strains were carried out as described previously. [91, 92]

Plasmid construction. All primers were designed using MacVector Version 14.5.2 (MacVector, Inc.) and synthesized by Eurofins MWG, Germany. All plasmids were confirmed by sequencing. Construction of expression-plasmid pTA1205 for 6xHis-

ADH2 expression and deletion-plasmids pTA1229 and pTA1230 for the deletion of adh1 and adh2 genes, respectively, were described previously. [29]

Strain construction. *H. volcanii* ΔadH1, ΔadH2, ΔtnaA and ΔgabT1 mutant strains were generated using previously described gene knock-out systems [91, 93]. *H. volcanii* strain H1895 (ΔpyrE2, Nph-pitA, Δmrr, ΔhdrB, Cdc48d-Ct, ΔpilB3C3, [94] was the source strain for generating the expression strain H2974 (ΔpyrE2, Nph-pitA, Δmrr, ΔhdrB, Cdc48d-Ct, ΔpilB3C3, ΔadH1, ΔadH2, ΔtnaA, ΔgabT1. Deletions were confirmed using Colony Hybridisation and Southern blot. The *H. volcanii* strain H2974 was transformed with pTA1205 to obtain strain H3094 (ΔpyrE2, Nph-pitA, Δmrr, ΔhdrB, Cdc48d-Ct, ΔpilB3C3, ΔadH1, ΔadH2, ΔtnaA, ΔgabT1) for overexpression of 6xHis-ADH2.

Protein expression and purification. An overnight starter culture (5 ml) was diluted (1:100) at OD_{600} ~ 0.1 into 5ml and again grown until OD_{600} ~ 0.1. Cultures were diluted 1:100 in 50 ml and incubated for 24 h at 150 rpm until an OD_{600} of ~ 0.5 was reached. Cultures were then diluted (1:50) into 333 ml YPC broth and induced with 0.1 g tryptophan and incubated at 150 rpm until an OD_{600} of ~ 1.2- 1.5 was reached (24- 36 h). Cells were harvested by centrifugation and the resultant pellet was either frozen for later use or resuspended in 5 ml wash buffer (20 mM HEPES, pH 7.5, 2 M NaCl). Cells were disrupted by sonication on ice (~ 3x 30 s at 6 W) until the lysate appeared clear. After centrifugation (48000x g for 30 min, 4 °C) the supernatant was filtered and loaded onto a HisTrap HP (GE Healthcare) immobilised metal-chelate affinity chromatography (IMAC) column pre-charged with $NiSO_4$ (0.2 M) at a flow rate of 0.5 ml/min using loading buffer (20 mM HEPES, pH 7.5, 2 M NaCl, 20 mM imidazole). Elution buffer (20 mM HEPES, pH 7.5, 2 M NaCl, 50 mM EDTA) was applied to the IMAC column to obtain 2 ml fractions. Fractions were assayed spectrophotometrically for alcohol dehydrogenase activity. Selected fractions were pooled and then dialysed and concentrated using Viva Spin columns (Sartorius) using 3 M Glycine-KOH buffer, pH 8. Purified protein samples were analysed by SDS-PAGE and protein concentration was determined using the Bradford protein assay dye reagent (Bio-Rad Laboratories GmbH, Germany).

Activity assays. Relative specific activity was assayed spectrophotometrically by monitoring the increase in absorbance of the cofactor NADPH at 340 nm using an Epoch2 Microplate spectrophotometer (Biotek) with UV-transparent 96-well plates. The reaction mixture routinely contained ethanol (100 mM), $NADP^+$ (1 mM) and enzyme sample (~ 450 nM) and 50 mM Glycine-KOH, pH 10.0 buffer containing 4 M KCl. Experiments were carried out at 50 °C for 20 minutes.

Ionic Liquids. Ionic liquids used for experimental activity assays as well as MD simulations are summarised in SI, Table S1. For activity assays $[Me_3S]^+[MeSO_4]^-$, $[Tetrakis]^+[Cl]^-$, $[Choline]^+[Cl]^-$ and $[Choline]^+[Bitartrate]^-$ were purchased from Acros Organics. $[DiMIM]^+[MeSO_4]^-$ and $[P_{6,6,6,14}]^+[NTf_2]^-$ were purchased from Fluka. $[Me_3S]^+[NTf_2]^-$ was purchased from Solvent Innovation. $[BMIM]^+[MeOEtSO_4]^-$, $[N_{1,1,8,8}]^+[MeSO_4]^-$ and $[N_{4,1,1,1}]^+[(MeO)_2OPO]^-$ were donated by the Sustainable Process Technologies (SPT) group at University of Nottingham. $[P_{4,4,4,4}]^+[Cl]^-$ was purchased from QUILL. $[Me_3SO]^+[I]^-$ and $[Me_3S]^+[I]^-$ were purchased from Sigma Aldrich. All ionic liquids were used as received without further purification.

Characterisation of *Hv*ADH2 activity in ILs. All ionic liquid mixtures were made up in 50 mM Glycine-KOH, pH 10.0 buffer containing 4 M KCl, unless stated otherwise. Oxidative reactions of *Hv*ADH2 were assayed using 1-ethanol (100 mM) and $NADP^+$ (1 mM) in aqueous ionic liquid mixtures. For a detailed composition of mixtures see SI.

Protein Sequences and Structures. The protein sequence of *Hv*ADH2 was retrieved from the National Centre for Biotechnology (NCBI) database with deposit number ELY36761.1. Homology models were built using Swiss-Model, [95-99] Phyre2, [100] and I-TASSER. [101, 102] Models were assessed via structural alignment (BLAST) and Visualisation (PyMOL). The best model was selected based on the preservation of conserved residues of the catalytic triad coordinating the catalytic zinc (CYS-89, CYS-92, CYS-95 and CYS-103). Following this, the homology model from I-TASSER with the highest C-score (1.62) was chosen to build the tetrameric structure using BIOVIA Discovery Studios Visualizer. [103] The tetrameric structure of TADH from *Thermus Sp. Atn1* was retrieved from the protein data bank (RCSB) with the deposit reference 4cpd, and was used as a template to superimpose the monomeric model built by I-TASSER to obtain coordinate positions of the four homo-tetramer units. The

geometrically cleaned-up structure was then validated by PROCHECK. [104] The obtained Ramachandran plot reported the dihedral angles at 74.7 % in the most favoured region, 20.1 % in the allowed region, 2.8 % in the generously allowed region and 2.4 % in the disallowed region (see SI Figure S20). The model was then used to create necessary topology files and was processed with AMBER18 (Assisted Model Building with Energy Refinement), [105] as described below, to run MD simulations. From 200 ns MD time the root mean square deviation (RMSD) was calculated for backbone atoms to validate the model stability during simulation (SI Figure S21).

Molecular Dynamics Simulation and Preparation. The protonation states of amino acid side chains of the I-TASSER *Hv*ADH2 model were adjusted to pH 10 conditions using the H++ server. The software suite used for running all simulations was AMBER18, [105] whereby xLEaP, antechamber and parmchk were used as preparatory programs, pmemd.cuda 9.2 was used to run simulations and cpptraj was used to transform obtained trajectories for visualisation. The forcefield leaprc.ff14SB was used for non-coordinating protein residues and the Zinc Amber forcefield (ZAFF) [106] was used for Zn^{2+} coordinating residues, whereby CY4 and HD2 parameters were applied for catalytic residues and CY1 parameters were chosen for structural residues.

A recent study by Daronkola *et al*. found that unoptimized anion-cation parameters for the interaction of potassium with acetate applied in the Amber-GAFF force fields can misrepresent activity derivatives varying with concentration. [107] They found that contact-shared ion pairs (CIPs) are overestimated, while solvent-shared ion pairs (SIPs) are slightly underestimated. RDF values produced in their study with their newly chosen scaling factor showed the same peak position, but coordination numbers were overall lower for potassium around acetate compared to the amber scaling factor. They still found an increased proximal number density for K^+ ions and H_2O molecules around halophilic proteins when compared to their mesophilic counterparts. Use of the amber GAFF force field for the present study thus presents a limitation to quantitation that we acknowledge in the context of this finding. We have thus presented comparative data rather than quantitative, to ensure that our findings remain representative.

Ionic liquid structures were built in Avogadro [108] and structures were optimised with xLEaP using the forcefield leaprc.gaff with amber parameters sourced from

frcmod.ionsjc_tip4pew. Antechamber was used to calculate RESP charges, whereby the total charge of each ion was reduced by applying a factor 0.8 to all atomic charges of the individual ions according to evidence suggested in literature. [109] Packmol was used to assemble molecules for simulations in variable numbers reflecting different ion concentrations. [110] Molecule numbers were calculated according to $N_{ion}=N_A*c_{ion}(mol/l)*V(l)$, where N_{ions} is the number of ions, N_A is the Avogadro number ($6.022*10^{23}$), c_{ion} the concentration of the ion and V the volume. The protein structure was placed in a quadratic box (100x100x100 Å) and neutralised by adding K^+ and Cl^- ions using xLEaP. Following neutralisation, ionic liquid molecules were inserted to a concentration of 150 mM (a total number of 80 ion pairs) using packmol. In a final preparation step, the box was solvated with a minimum distance of 2 Å between water molecules using the TIP3P [111] water model in xLEaP and K^+ and Cl^- ions were added to a concentration of 4 M (total number was around 1800) using the *addionsrand* command.

Long-range electrostatic interactions and non-bonded interactions were modelled using the particle-mesh Ewald method for periodic boundaries with a cut-off of 10 Å. The first energy minimisation run (50,000,000 steps, steepest descent algorithm for the first 20,000,000 steps, then switched to conjugate gradient algorithm) was performed only on water with a restrain force of 10 kcal/mol to all other molecules. This was followed by a first heating step of 10 ps to 323.1 5K applied to water molecules and a restrain force of 10 kcal/mol to all other molecules. The overall system was integrated to a temperature isotherm using the Berendsen thermostat with a close coupling of 0.5 ps. A second minimisation step was performed and applied to all atoms using no restraints, followed by a second heating step of the whole system for 0.25 ns under NPT conditions (constant volume in periodic boundaries, Berendsen thermostat) and a subsequent density equilibration step applying Langevin dynamics for 2.5 ns under NTP conditions (constant pressure in periodic boundaries) with restrain forces of 10 kcal/mol to the protein. Molecular dynamics production run simulations were subsequently run with unrestrained systems for between 150 and 200 ns.

Analysis of MD Simulations. Trajectories were visualised using VMD. [112] The physical parameters RMSD, [113, 114] SP [115] and RDFs were calculated using python package MDAnalysis [116, 117]. Principle component analyses on Cα atoms to obtain eigenvalues and eigenvectors were calculated using GROMACS [118, 119]

and the first two eigenvectors, PC1 and PC2, which describe > 55 % of the structural transitions of the overall protein for every system were used to construct free energy landscapes. Post analysis of the molecular dynamics data was graphically represented with Matlab and python packages (MDAnalysis, matplotlib, numpy). TRAVIS was used to calculate SDFs, [120] which were visualised in VMD with isovalues 10 for water and 3 for potassium.

Calculations of local properties and descriptors. The molecular electrostatic potential range (MEP_{range}) and the polarizability for IL cations and anions were calculated using the Cepos Insilico software packages EMPIRE. [121] Cube files were obtained through eh5cube.sh off the EMPIRE wavefunction output file and visualised in VMD with isovalues of ~ 0.02 e $Å^{-3}$.

References

1. Simić, S., et al., *Shortening Synthetic Routes to Small Molecule Active Pharmaceutical Ingredients Employing Biocatalytic Methods.* Chemical Reviews, 2021. **122**(1): p. 1052-1126.
2. Chapman, J., A. Ismail, and C. Dinu, *Industrial Applications of Enzymes: Recent Advances, Techniques, and Outlooks.* Catalysts, 2018. **8**(6): p. 238.
3. Hertwich, E.G., et al., *Integrated life-cycle assessment of electricity-supply scenarios confirms global environmental benefit of low-carbon technologies.* Proceedings of the National Academy of Sciences, 2014. **112**(20): p. 6277-6282.
4. Volkamer, R., et al., *Secondary organic aerosol formation from anthropogenic air pollution: Rapid and higher than expected.* Geophysical Research Letters, 2006. **33**(17).
5. Schindl, A., et al., *Proteins in Ionic Liquids: Reactions, Applications, and Futures.* Frontiers in Chemistry, 2019. **7**.
6. Hagen, M.L., J.B. Harper, and A.K. Croft, *Recent advances in the use of ionic liquids as solvents for protein-based materials and chemistry.* Current Opinion in Green and Sustainable Chemistry, 2022. **36**: p. 100637.
7. Byrne, N., et al., *Reversible folding--unfolding, aggregation protection, and multi-year stabilization, in high concentration protein solutions, using ionic liquids.* Chem. Commun., 2007: p. 2714-2716.
8. Summers, S., et al., *Enhanced Activity and Stability of Acidothermus cellulolyticus Endoglucanase 1 in Ionic Liquids via Engineering Active Site Residues and Non-Native Disulfide Bridges.* ACS Sustainable Chemistry & Engineering, 2020. **8**(30): p. 11299--11307.
9. Shin, D.W., et al., *Enhanced lipase-catalyzed synthesis of sugar fatty acid esters using supersaturated sugar solution in ionic liquids.* Enzyme and Microbial Technology, 2019. **126**: p. 18-23.
10. Jarin, Z. and J. Pfaendtner, *Ionic Liquids Can Selectively Change the Conformational Free-Energy Landscape of Sugar Rings.* Journal of Chemical Theory and Computation, 2014. **10**(2): p. 507--510.
11. Alvarez, E., et al., *Clean Enzymatic Production of Flavor Esters in Spongelike Ionic Liquids.* ACS Sustainable Chemistry & Engineering, 2019. **7**(15): p. 13307--13314.
12. Villa, R., et al., *Ionic liquids as an enabling tool to integrate reaction and separation processes.* Green Chem., 2019. **21**: p. 6527-6544.
13. Villa, R., et al., *Chapter 14 - Biocatalytic processes in ionic liquids and supercritical carbon dioxide biphasic systems*, in *Biocatalysis in Green Solvents*, P. Lozano, Editor. 2022, Academic Press. p. 403-433.
14. Schuliger, J.W., *Purification and characterization of a novel amylolytic enzyme from ES 4, a marine hyperthermophilic archaeum.*, S.H. Brown, Editor. 1993, *Molecular Marine Biology and Biotechnology*. p. 76-87.
15. Falb, M., et al., *Living with two extremes: Conclusions from the genome sequence of Natronomonas pharaonis.* Genome Research, 2005. **15**(10): p. 1336-1343.
16. Mevarech, M., F. Frolow, and L.M. Gloss, *Halophilic enzymes: proteins with a grain of salt.* Biophysical Chemistry, 2000. **86**(2-3): p. 155-164.
17. Zhang, T., et al., *Identification of a haloalkaliphilic and thermostable cellulase with improved ionic liquid tolerance.* Green Chemistry, 2011. **13**(8): p. 2083.

18. Gunny, A.A.N., et al., *Potential halophilic cellulases for in situ enzymatic saccharification of ionic liquids pretreated lignocelluloses.* Bioresource Technology, 2014. **155**: p. 177-181.
19. Zhao, B., et al., *Efficient enzymatic saccharification of alkaline and ionic liquid-pretreated bamboo by highly active extremozymes produced by the co-culture of two halophilic fungi.* Bioresource Technology, 2021. **319**: p. 124115.
20. Raddadi, N., et al., *Halo-alkalitolerant and thermostable cellulases with improved tolerance to ionic liquids and organic solvents from Paenibacillus tarimensis isolated from the Chott El Fejej, Sahara desert, Tunisia.* Bioresource Technology, 2013. **150**: p. 121-128.
21. Ben Hmad, I. and A. Gargouri, *Ionic liquid-tolerant cellulase system of Stachybotrys microspora exploited in the in situ saccharification of lignocellulosic biomass.* Journal of Molecular Liquids, 2020. **310**: p. 113167.
22. Mesbah, N.M. and J. Wiegel, *A Halophilic, Alkalithermostable, Ionic Liquid-Tolerant Cellulase and Its Application in In Situ Saccharification of Rice Straw.* BioEnergy Research, 2017. **10**(2): p. 583-591.
23. Rezaei, S., A.R. Shahverdi, and M.A. Faramarzi, *Isolation, one-step affinity purification, and characterization of a polyextremotolerant laccase from the halophilic bacterium Aquisalibacillus elongatus and its application in the delignification of sugar beet pulp.* Bioresource Technology, 2017. **230**: p. 67-75.
24. Karbalaei-Heidari, H.R., M. Shahbazi, and G. Absalan, *Characterization of a Novel Organic Solvent Tolerant Protease from a Moderately Halophilic Bacterium and Its Behavior in Ionic Liquids.* Applied Biochemistry and Biotechnology, 2013. **170**(3): p. 573-586.
25. Liu, K., et al., *Effect of ionic liquids on catalytic characteristics of hyperthermophilic and halophilic phenylalanine dehydrogenase and mechanism study.* Biochemical Engineering Journal, 2021. **176**: p. 108175.
26. Ji, Z., et al., *Design of robust malate dehydrogenases by assembly of motifs of halophilic and thermophilic enzyme based on interaction network.* Biochemical Engineering Journal, 2023. **190**: p. 108758.
27. Dym, O., M. Mevarech, and J.L. Sussman, *Structural Features That Stabilize Halophilic Malate Dehydrogenase from an Archaebacterium.* Science, 1995. **267**(5202): p. 1344-1346.
28. Ng, W.V., et al., *Genome sequence of Halobacterium species NRC-1.* Proceedings of the National Academy of Sciences, 2000. **97**(22): p. 12176-12181.
29. Timpson, L.M., et al., *A comparison of two novel alcohol dehydrogenase enzymes (ADH1 and ADH2) from the extreme halophile Haloferax volcanii.* Applied Microbiology and Biotechnology, 2012. **97**(1): p. 195-203.
30. Alsafadi, D., S. Alsalman, and F. Paradisi, *Extreme halophilic alcohol dehydrogenase mediated highly efficient syntheses of enantiopure aromatic alcohols.* Organic & Biomolecular Chemistry, 2017. **15**(43): p. 9169-9175.
31. Alsafadi, D. and F. Paradisi, *Effect of organic solvents on the activity and stability of halophilic alcohol dehydrogenase (ADH2) from Haloferax volcanii.* Extremophiles, 2012. **17**(1): p. 115-122.
32. Nordwald, E.M. and J.L. Kaar, *Stabilization of enzymes in ionic liquids via modification of enzyme charge.* Biotechnology and Bioengineering, 2013. **110**(9): p. 2352-2360.
33. Jaeger, V., P. Burney, and J. Pfaendtner, *Comparison of Three Ionic Liquid-Tolerant Cellulases by Molecular Dynamics.* Biophysical Journal, 2015. **108**(4): p. 880-892.
34. Mohammadyazdani, N., M.R. Bozorgmehr, and M. Momen-Heravi, *Conformation changes and diffusion of α-amylase in 1-hexyle-3-methylimidazolium chloride ionic*

liquid: A molecular dynamics simulation perspective. Journal of Molecular Liquids, 2016. **221**: p. 463-468.
35. Tung, H.-J. and J. Pfaendtner, *Kinetics and mechanism of ionic-liquid induced protein unfolding: application to the model protein HP35.* Molecular Systems Design & Engineering, 2016. **1**(4): p. 382-390.
36. Zhao, J., et al., *Ionic liquid activatedBacillus subtilislipase A variants through cooperative surface substitutions.* Biotechnology and Bioengineering, 2015. **112**(10): p. 1997-2004.
37. Zhao, J., et al., *Unraveling the effects of amino acid substitutions enhancing lipase resistance to an ionic liquid: a molecular dynamics study.* Physical Chemistry Chemical Physics, 2018. **20**(14): p. 9600-9609.
38. Jafari, M., et al., *Molecular level insight into stability, activity, and structure of Laccase in aqueous ionic liquid and organic solvents: An experimental and computational research.* Journal of Molecular Liquids, 2020. **317**: p. 113925.
39. Micaêlo, N.M. and C.M. Soares, *Protein Structure and Dynamics in Ionic Liquids. Insights from Molecular Dynamics Simulation Studies.* The Journal of Physical Chemistry B, 2008. **112**(9): p. 2566-2572.
40. Shao, Q., *On the influence of hydrated imidazolium-based ionic liquid on protein structure stability: A molecular dynamics simulation study.* The Journal of Chemical Physics, 2013. **139**(11): p. 115102.
41. Kim, H.S., et al., *The relationship between enhanced enzyme activity and structural dynamics in ionic liquids: a combined computational and experimental study.* Physical Chemistry Chemical Physics, 2014. **16**(7): p. 2944.
42. Haberler, M., C. Schröder, and O. Steinhauser, *Solvation studies of a zinc finger protein in hydrated ionic liquids.* Physical Chemistry Chemical Physics, 2011. **13**(15): p. 6955.
43. Figueiredo, A.M., et al., *Protein destabilisation in ionic liquids: the role of preferential interactions in denaturation.* Physical Chemistry Chemical Physics, 2013. **15**(45): p. 19632.
44. Ghosh, S., et al., *Ionic liquid induced dehydration and domain closure in lysozyme: FCS and MD simulation.* The Journal of Chemical Physics, 2015. **143**(12): p. 125103.
45. Ghorbani, S.M., M.R. Housaindokht, and M.R. Bozorgmehr, *Investigating the effect of 1-Butyl-3-methylimidazolium bromide and 1-Butyl-3-methylimidazolium methyl sulfate ionic liquids on structure and function of Chloroproxidase by molecular dynamics simulation.* Journal of Molecular Liquids, 2021. **332**: p. 115850.
46. Ghanbari-Ardestani, S., et al., *The effect of different percentages of triethanolammonium butyrate ionic liquid on the structure and activity of urate oxidase: Molecular docking, molecular dynamics simulation, and experimental study.* Journal of Molecular Liquids, 2019. **292**: p. 111318.
47. Ghanta, K.P., et al., *Microscopic Understanding of the Effect of Ionic Liquid on Protein from Molecular Simulation Studies.* The Journal of Physical Chemistry B, 2020. **124**(19): p. 3909-3921.
48. Janati-Fard, F., et al., *The influence of two imidazolium-based ionic liquids on the structure and activity of glucose oxidase: Experimental and theoretical studies.* International Journal of Biological Macromolecules, 2018. **114**: p. 656-665.
49. Ghaedizadeh, S., et al., *Understanding the molecular behaviour of Renilla luciferase in imidazolium-based ionic liquids, a new model for the α/β fold collapse.* Biochemical Engineering Journal, 2016. **105**: p. 505-513.
50. Tarannum, A., et al., *Role of Preferential Ions of Ammonium Ionic Liquid in Destabilization of Collagen.* The Journal of Physical Chemistry B, 2016. **120**(27): p. 6515-6524.

51. Singh, O., et al., *Dual mechanism of ionic liquid-induced protein unfolding.* Physical Chemistry Chemical Physics, 2020. **22**(35): p. 19779-19786.
52. Gäding, J., et al., *Impact of confinement and polarizability on dynamics of ionic liquids.* The Journal of Chemical Physics, 2022. **156**(6): p. 064703.
53. Schindl, A., et al., *Controlling the outcome of SN2 reactions in ionic liquids: from rational data set design to predictive linear regression models.* Phys. Chem. Chem. Phys., 2020. **22**: p. 23009-23018.
54. Dabirmanesh, B., et al., *Inhibition mediated stabilization effect of imidazolium based ionic liquids on alcohol dehydrogenase.* Journal of Molecular Liquids, 2012. **170**: p. 66-71.
55. Zhang, Y., X. Huang, and Y. Li, *Negative effect of [bmim][PF6] on the catalytic activity of alcohol dehydrogenase: mechanism and prevention.* Journal of Chemical Technology & Biotechnology, 2008. **83**(9): p. 1230-1235.
56. de Gonzalo, G., et al., *Asymmetric biocatalytic reduction of ketones using hydroxy-functionalised water-miscible ionic liquids as solvents.* Tetrahedron: Asymmetry, 2007. **18**(21): p. 2541-2546.
57. Kohlmann, C., et al., *Ionic liquid facilitates biocatalytic conversion of hardly water soluble ketones.* Journal of Molecular Catalysis B: Enzymatic, 2011. **68**(2): p. 147-153.
58. Musa, M.M., Ziegelmann-Fjeld, K. I., Vieille, C., and Phillips, R. S., *Activity and selectivity of w110a secondary alcohol dehydrogenase from Thermoanaerobacter ethanolicus in organic solvents and ionic liquids: Mono- and biphasic media.* Org. Biomol. Chem. , 2008. **6**: p. 887–892.
59. Shi, X.-A., M.-H. Zong, and W.-Y. Lou, *Effect of Ionic Liquids on Catalytic Characteristics of Horse Liver Alcohol Dehydrogenase.* Chinese Journal of Chemistry, 2006. **24**(11): p. 1643-1647.
60. Haberler, M. and O. Steinhauser, *On the influence of hydrated ionic liquids on the dynamical structure of model proteins: a computational study.* Physical Chemistry Chemical Physics, 2011. **13**(40): p. 17994.
61. Haberler, M., C. Schröder, and O. Steinhauser, *Hydrated Ionic Liquids with and without Solute: The Influence of Water Content and Protein Solutes.* Journal of Chemical Theory and Computation, 2012. **8**(10): p. 3911-3928.
62. Lenton, S., et al., *Structural evidence for solvent-stabilisation by aspartic acid as a mechanism for halophilic protein stability in high salt concentrations.* Physical Chemistry Chemical Physics, 2016. **18**(27): p. 18054-18062.
63. Talon, R., et al., *An experimental point of view on hydration/solvation in halophilic proteins.* Frontiers in Microbiology, 2014. **5**.
64. Britton, K.L., et al., *Analysis of protein solvent interactions in glucose dehydrogenase from the extreme halophile Haloferax mediterranei.* Proceedings of the National Academy of Sciences, 2006. **103**(13): p. 4846-4851.
65. Warden, A.C., et al., *Rational engineering of a mesohalophilic carbonic anhydrase to an extreme halotolerant biocatalyst.* Nature Communications, 2015. **6**(1).
66. Dahanayake, J.N. and K.R. Mitchell-Koch, *Entropy connects water structure and dynamics in protein hydration layer.* Physical Chemistry Chemical Physics, 2018. **20**(21): p. 14765-14777.
67. Madern, D., C. Ebel, and G. Zaccai, *Halophilic adaptation of enzymes.* Extremophiles, 2000. **4**(2): p. 91-98.
68. Thomas, A.S. and A.H. Elcock, *Molecular Dynamics Simulations of Hydrophobic Associations in Aqueous Salt Solutions Indicate a Connection between Water Hydrogen Bonding and the Hofmeister Effect.* Journal of the American Chemical Society, 2007. **129**(48): p. 14887-14898.

69. Zangi, R., M. Hagen, and B.J. Berne, *Effect of Ions on the Hydrophobic Interaction between Two Plates.* Journal of the American Chemical Society, 2007. **129**(15): p. 4678-4686.
70. Breslow, R., *Hydrophobic effects on simple organic reactions in water.* Accounts of Chemical Research, 1991. **24**(6): p. 159-164.
71. Blokzijl, W. and J.B.F.N. Engberts, *Hydrophobic Effects. Opinions and Facts.* Angewandte Chemie International Edition in English, 1993. **32**(11): p. 1545-1579.
72. Jäger, C.M., et al., *Counterions Control the Self-Assembly of Structurally Persistent Micelles: Theoretical Prediction and Experimental Observation of Stabilization by Sodium Ions.* Chemistry – A European Journal, 2009. **15**(34): p. 8586-8592.
73. Rosenlehner, K., et al., *Sodium Effect on Self-Organization of Amphiphilic Carboxylates: Formation of Structured Micelles and Superlattices.* Chemistry – A European Journal, 2010. **16**(31): p. 9544-9554.
74. Mevarech, M., F. Frolow, and L.M. Gloss, *Halophilic enzymes: proteins with a grain of salt.* Biophysical Chemistry, 2000. **86**(2-3): p. 155--164.
75. Bešter-Rogač, M., A. Stoppa, and R. Buchner, *Ion Association of Imidazolium Ionic Liquids in Acetonitrile.* The Journal of Physical Chemistry B, 2014. **118**(5): p. 1426-1435.
76. Laage, D., et al., *Reorientation and Allied Dynamics in Water and Aqueous Solutions.* Annual Review of Physical Chemistry, 2011. **62**(1): p. 395-416.
77. Bottari, C., et al., *Interfacial Water and Microheterogeneity in Aqueous Solutions of Ionic Liquids.* The Journal of Physical Chemistry B, 2022. **126**(23): p. 4299--4308.
78. Schröder, C., et al., *Collective rotational dynamics in ionic liquids: A computational and experimental study of 1-butyl-3-methyl-imidazolium tetrafluoroborate.* The Journal of Chemical Physics, 2007. **126**(8): p. 084511.
79. Tariq, M., et al., *Surface tension of ionic liquids and ionic liquid solutions.* Chem. Soc. Rev., 2012. **41**(2): p. 829-868.
80. Fernandez-Alvaro, E. and P. Domínguez de Maria, *Ionic Liquids in Biocatalytic Oxidations: From Non-conventional Media to Non-solvent Applications.* Current Organic Chemistry, 2012. **16**(21): p. 2492-2507.
81. Nagel, Z.D., S. Cun, and J.P. Klinman, *Identification of a Long-range Protein Network That Modulates Active Site Dynamics in Extremophilic Alcohol Dehydrogenases.* Journal of Biological Chemistry, 2013. **288**(20): p. 14087-14097.
82. Aguilar, C.F., et al., *Crystal structure of the β-glycosidase from the hyperthermophilic archeon Sulfolobus solfataricus: resilience as a key factor in thermostability.* Journal of Molecular Biology, 1997. **271**(5): p. 789-802.
83. Hennig, M., et al., *2.0 åstructure of indole-3-glycerol phosphate synthase from the hyperthermophile Sulfolobus solfataricus: possible determinants of protein stability.* Structure, 1995. **3**(12): p. 1295-1306.
84. Villeret, V., et al., *The crystal structure of Pyrococcus furiosus ornithine carbamoyltransferase reveals a key role for oligomerization in enzyme stability at extremely high temperatures.* Proceedings of the National Academy of Sciences, 1998. **95**(6): p. 2801-2806.
85. Frolow, F., et al., *Insights into protein adaptation to a saturated salt environment from the crystal structure of a halophilic 2Fe-2S ferredoxin.* Nature Structural Biology, 1996. **3**(5): p. 452-458.
86. Arai, S., et al., *Structure of a highly acidic β-lactamase from the moderate halophileChromohalobactersp. 560 and the discovery of a Cs$^+$-selective binding site.* Acta Crystallographica Section D Biological Crystallography, 2015. **71**(3): p. 541-554.

87. Datta, S., et al., *Ionic liquid tolerant hyperthermophilic cellulases for biomass pretreatment and hydrolysis.* Green Chemistry, 2010. **12**(2): p. 338.
88. Sthoer, A.P.A. and E.C. Tyrode, *Anion Specific Effects at Negatively Charged Interfaces: Influence of Cl$^--$, Br$^--$, I$^--$, and SCN$^--$ on the Interactions of Na$^+$ with the Carboxylic Acid Moiety.* The Journal of Physical Chemistry B, 2021. **125**(44): p. 12384-12391.
89. Hunger, J., et al., *Nature of Cations Critically Affects Water at the Negatively Charged Silica Interface.* Journal of the American Chemical Society, 2022. **144**(43): p. 19726-19738.
90. Guy, C.P., et al., *Interactions of RadB, a DNA Repair Protein in Archaea, with DNA and ATP.* Journal of Molecular Biology, 2006. **358**(1): p. 46-56.
91. Allers, T., et al., *Development of Additional Selectable Markers for the Halophilic Archaeon Haloferax volcanii Based on the leuB and trpA Genes.* Applied and Environmental Microbiology, 2004. **70**(2): p. 943-953.
92. Norais, C., et al., *Genetic and Physical Mapping of DNA Replication Origins in Haloferax volcanii.* PLoS Genetics, 2007. **3**(5): p. e77.
93. Bitan-Banin, G., R. Ortenberg, and M. Mevarech, *Development of a Gene Knockout System for the Halophilic Archaeon Haloferax volcanii by Use of the pyrE Gene.* Journal of Bacteriology, 2003. **185**(3): p. 772-778.
94. Strillinger, E., et al., *Production of halophilic proteins using Haloferax volcanii H1895 in a stirred-tank bioreactor.* Applied Microbiology and Biotechnology, 2015. **100**(3): p. 1183-1195.
95. Waterhouse, A., et al., *SWISS-MODEL: homology modelling of protein structures and complexes.* Nucleic Acids Research, 2018. **46**(W1): p. W296--W303.
96. Bienert, S., et al., *The SWISS-MODEL Repository---new features and functionality.* Nucleic Acids Research, 2017. **45**(D1): p. D313--D319.
97. Guex, N., M.C. Peitsch, and T. Schwede, *Automated comparative protein structure modeling with SWISS-MODEL and Swiss-PdbViewer: A historical perspective.* ELECTROPHORESIS, 2009. **30**(S1): p. S162--S173.
98. Studer, G., et al., *ProMod3---A versatile homology modelling toolbox.* PLOS Computational Biology, 2021. **17**(1): p. e1008667--.
99. Benkert, P., M. Biasini, and T. Schwede, *Toward the estimation of the absolute quality of individual protein structure models.* Bioinformatics, 2011. **27**(3): p. 343--350.
100. Kelley, L.A., et al., *The Phyre2 web portal for protein modeling, prediction and analysis.* Nature Protocols, 2015. **10**(6): p. 845--858.
101. Zhang, Y., *I-TASSER server for protein 3D structure prediction.* BMC Bioinformatics, 2008. **9**(1): p. 40.
102. Yang, J., et al., *The I-TASSER Suite: protein structure and function prediction.* Nature Methods, 2015. **12**(1): p. 7--8.
103. Biovia, D.S., *DS Materials Studio, 16.1. 0.21.* 2018.
104. Colovos, C. and T.O. Yeates, *Verification of protein structures: Patterns of nonbonded atomic interactions.* Protein Science, 1993. **2**(9): p. 1511-1519.
105. Lee, T.-S., et al., *GPU-Accelerated Molecular Dynamics and Free Energy Methods in Amber18: Performance Enhancements and New Features.* Journal of Chemical Information and Modeling, 2018. **58**(10): p. 2043--2050.
106. Peters, M.B., et al., *Structural Survey of Zinc-Containing Proteins and Development of the Zinc AMBER Force Field (ZAFF).* Journal of Chemical Theory and Computation, 2010. **6**(9): p. 2935-2947.
107. Geraili Daronkola, H. and A. Vila Verde, *Proteins maintain hydration at high [KCl] concentration regardless of content in acidic amino acids.* Biophysical Journal, 2021. **120**(13): p. 2746-2762.

108. Hanwell, M.D., et al., *Avogadro: an advanced semantic chemical editor, visualization, and analysis platform.* Journal of Cheminformatics, 2012. **4**(1).
109. Sprenger, K.G., V.W. Jaeger, and J. Pfaendtner, *The General AMBER Force Field (GAFF) Can Accurately Predict Thermodynamic and Transport Properties of Many Ionic Liquids.* The Journal of Physical Chemistry B, 2015. **119**(18): p. 5882-5895.
110. Martínez, L., et al., *PACKMOL: A package for building initial configurations for molecular dynamics simulations.* Journal of Computational Chemistry, 2009. **30**(13): p. 2157-2164.
111. Jorgensen, W.L., et al., *Comparison of simple potential functions for simulating liquid water.* The Journal of Chemical Physics, 1983. **79**(2): p. 926-935.
112. Humphrey, W., A. Dalke, and K. Schulten, *VMD: Visual molecular dynamics.* Journal of Molecular Graphics, 1996. **14**(1): p. 33-38.
113. Theobald, D.L., *Rapid calculation of RMSDs using a quaternion-based characteristic polynomial.* Acta Crystallographica Section A Foundations of Crystallography, 2005. **61**(4): p. 478-480.
114. Liu, P., D.K. Agrafiotis, and D.L. Theobald, *Fast determination of the optimal rotational matrix for macromolecular superpositions.* Journal of Computational Chemistry, 2009. **31**(7): p. 1561-1563.
115. Araya-Secchi, R., et al., *Characterization of a Novel Water Pocket Inside the Human Cx26 Hemichannel Structure.* Biophysical Journal, 2014. **107**(3): p. 599-612.
116. Michaud-Agrawal, N., et al., *MDAnalysis: A toolkit for the analysis of molecular dynamics simulations.* Journal of Computational Chemistry, 2011. **32**(10): p. 2319-2327.
117. Gowers, R., et al., *MDAnalysis: A Python Package for the Rapid Analysis of Molecular Dynamics Simulations*, in *Proceedings of the Python in Science Conference*. 2016, SciPy.
118. Van Der Spoel, D., Lindahl, E., Hess, B., Groenhof, G., Mark, A. E., & Berendsen, H. J., *GROMACS: fast, flexible, and free.* 2005, *Journal of computational chemistry*. p. 1701-1718.
119. Lindahl, E., Hess, B., & Van Der Spoel, D., *GROMACS 3.0: a package for molecular simulation and trajectory analysis.* 2001, *Molecular modeling annual*. p. 306-317.
120. Brehm, M. and B. Kirchner, *TRAVIS - A Free Analyzer and Visualizer for Monte Carlo and Molecular Dynamics Trajectories.* Journal of Chemical Information and Modeling, 2011. **51**(8): p. 2007-2023.
121. Clark, M.T., *Cepos InSilico GmbH.* 2020.